UNIVERSIDADE D
COIMBRA

Leonardo Pappas Toscano Costa

ANÁLISE NUMÉRICA DE COLUNAS COMPOSTAS EM AÇO ENFORMADO A FRIO EM SITUAÇÃO DE INCÊNDIO

Dissertação de Mestrado Integrado em Engenharia Civil, na área de Especialização em Mecânica Estrutural, orientada pelo Professor Doutor Hélder David da Silva Craveiro pela Professora Doutora Aldina Maria da Cruz Santiago e apresentada ao Departamento de Engenharia Civil da Faculdade de Ciências e Tecnologia da Universidade de Coimbra.

Setembro de 2023

Faculdade de Ciências e Tecnologia da Universidade de Coimbra
Departamento de Engenharia Civil

Leonardo Pappas Toscano Costa

Análise numérica de colunas compostas em aço enformado a frio em situação de incêndio

Numerical analysis of closed built-up cold-formed steel columns in fire scenario

Dissertação de Mestrado Integrado em Engenharia Civil / Ambiente, na área de Especialização em Mecânica Estrutural, orientada pelo Professor Doutor Hélder David da Silva Craveiro e pela Professora Doutora Aldina Maria da Cruz Santiago

Setembro de 2023

1 2 9 0

UNIVERSIDADE D
COIMBRA

AGRADECIMENTOS

Esta é a ocasião ideal para deixar registrada a minha gratidão àqueles que me possibilitaram a incrível experiência de estudar em Coimbra: meus pais, avós e irmãos. Agradeço por todos os sacrifícios que tenham feito e espero tê-los deixado orgulhosos.

Agradeço ao Professor Doutor Hélder Craveiro, que aceitou me orientar neste percurso e o fez mostrando uma disponibilidade ímpar (provavelmente mais até do que deveria).

Agradeço aos professores desta casa, que tanto instigaram a minha admiração pela Engenharia Civil. Carregarei o DEC com muito carinho para a vida profissional.

Agradeço aos meus amigos, tanto os que deixei em Brasília, quanto os que fiz na Europa. Em especial à Gabriela Lima, Pedro Assef, Guilherme Tassari e Gabriel Cathoud.

Agradeço, por fim, a todos os desafios que me foram postos. Esses me possibilitaram aprender e crescer.

"Primeiro as primeiras coisas"

Fernando Toscano Costa

RESUMO

A adaptabilidade dos perfis de aço enformados a frio permite combinar várias perfis individuais para criar secções compostas com capacidades de carga muito maiores, tornando-os um forte concorrente no sector da construção. Esta tese foi elaborada para pormenorizar os modelos numéricos paramétricos que avaliam o comportamento de pilares de aço enformado a frio com secção fechada em cenário de incêndio, bem como os resultados decorrentes. Para criar 80 provetes virtuais, os parâmetros a variar foram: secção transversal (quatro configurações diferentes usando os perfis C, U e Σ), comprimento (1050 mm e 3000 mm), nível de carga (30% e 50% da capacidade de carga à temperatura ambiente) e espaçamento dos conetores (cinco para cada comprimento). O principal objetivo era investigar o impacto do espaçamento quando os pilares eram sujeitos ao fogo, pelo que o nível de serviço foi calibrado para que todos os pilares colapsassem à mesma temperatura crítica. Com uma base de comparação — a temperatura — a carga de colapso foi comparada dentre os espaçamentos. Verificou-se que o espaçamento pode reduzir a capacidade de carga até 25,7%, quando comparado com a configuração com conexão perfeita. Outro objetivo da investigação foi verificar a exatidão das previsões do Eurocódigo relativamente à temperatura crítica. Dividindo o método do Eurocódigo em duas partes: a capacidade de carga à temperatura ambiente e o mecanismo iterativo da temperatura crítica, verificou-se que este último não é muito bom, enquanto o primeiro é mau e o menos fiável dos dois. Uma vez que a segunda parte depende da primeira, em conjunto, podem gerar uma previsão que, em alguns casos, está com 31,6% de erro.

Palavras-Chave: Aço Enformado a Frio, Seções Compostas Fechadas, Incêndio, Colunas, Encurvadura, Espaçamento, Ação Compósita

ABSTRACT

Cold-formed steel sections' adaptability makes it possible to combine various individual sections to create built-up components with much larger load-bearing capacities, making it a strong contender in the construction sector. This thesis was elaborated to detail the numerical parametric models that assess the behavior of CFS closed built-up columns in fire scenario, as well as the ensuing results. To create 80 virtual specimens, the varying parameters were: cross-section (four different configurations using the C, U and Σ channels), length (1050 mm and 3000 mm), load level (30% and 50% of the ambient temperature load bearing capacity) and fastener's spacing (five for each length). The main goal was to investigate the impact of the spacing when the columns were subjected to fire, so the service level was calibrated to make every column collapse at the same critical temperature. With a ground of comparison — the temperature — the collapse load was compared. It was found that the spacing can reduce the load capacity up to 25.7%, when compared to the configuration with perfect connection. Another objective of the research was to see how accurate the Eurocode's predictions were regarding critical temperature. Dividing the Eurocode's method in two parts: the load bearing capacity at ambient temperature and the iterative critical temperature mechanism, it was found that the latter is not good enough, while the former is bad and the least reliable of the two. Since the second part depends on the first, together they can generate a prediction that is 31.6% off-target, in some instances.

Keywords: Cold-Formed Steel, Closed Built-Up Cross-Sections, Fire, Columns, Buckling, Spacing, Composite Action

TABLE OF CONTENTS

ABBREVIATIONS

CFS – Cold-Formed Steel

DSM – Direct Strength Method

EWM – Effective Width Method

FEA – Finite Elements Analysis

FEM – Finite Elements Model

GMNIA – Geometrically and Materially Nonlinear Analysis with Imperfections Included

HT – Heat Transfer

LBA – Linear Buckling Analysis

LSF – Light Steel Frame

NOTATION

Uppercase Latin

A – Area of a cross-section

A_{eff} – Effective area of a cross-section

E – Young's Modulus

$E_{fi,d}$ – Design effect of actions for the fire design situation

f_p – Steel proportional limit

f_u – Steel ultimate strength

f_y – Steel yield strength

G_k – Characteristic value of a permanent action

I – Moment of inertia

$k_{E,\theta}$ – Reduction factor for the slope of the linear elastic range at temperature θ

$k_{y,\theta}$ – Reduction factor for effective yield strength at temperature θ

L_e – Effective length of a member

$N_{b,Rd}$ – Design Buckling Resistance

$N_{b,fi,\theta,Rd}$ – Design buckling resistance at temperature θ of a compression member

N_{cr} – Elastic buckling force

$N_{cr,F}$ – Elastic flexural buckling force

$N_{cr,T}$ – Elastic torsional buckling force

$N_{cr,FT}$ – Elastic torsional–flexural buckling force

$Q_{k,1}$ – Characteristic value of the leading variable action

$R_{fi,d,t}$ – Design resistance of the steel member, for the fire design situation, at time t

Lowercase Latin

b – Width of a cross-section, plate width

b_e, b_{eff} – Effective width of a cross-section, effective plate width

d_i – Imperfection readings at different locations

h_e – Effective height of a cross-section

k_σ – Buckling factor depending on the stress distribution and boundary conditions of the plate

r – Radius of gyration of a cross-section

t – Plate thickness; time

Lowercase Greek

α – Imperfection factor

γ_G – Partial factor for permanent actions

γ_{M1} – Partial factor at ambient temperature

$\gamma_{M,fi}$ – Partial factor for the relevant material property, for the fire situation

$\gamma_{Q,1}$ – Partial factor for variable action 1

η_{fi} – Reduction factor for the design load level for the fire situation

θ_a – Steel temperature

$\theta_{a,cr}$ – Steel critical temperature

$\bar{\lambda}$ – Non-dimensional slenderness

μ_0 – Degree of utilization of the cross-section

ν – Poisson's Ratio

ρ – Reduction factor for plate buckling

σ – Stefan-Boltzmann constant

σ_{cr} – Elastic critical plate buckling stress

$\sigma_{cr,s}$ – Elastic critical buckling stress for an edge stiffener

φ – Resistance factor

χ – Reduction coefficient for the relevant buckling mode

χ_d – Reduction coefficient for the distortional buckling resistance

χ_{fi} – Reduction factor for f1exural buckling in the fire design situation

ψ_{fi} – Combination factor

1 INTRODUCTION

1.1 General considerations

In today's construction sector, cold-formed steel (CFS) has gained significant importance as a versatile and competitive material. Its advantages and diverse applications make it a preferred choice for various construction projects.

CFS offers several key advantages over other construction materials. Firstly, its lightweight nature enables easy handling, transportation, and installation, leading to improved efficiency, reduced construction time and smaller environmental impact (Vitale et al., 2018). Additionally, CFS exhibits excellent structural performance, including high strength-to-weight ratio and resistance to seismic forces, making it suitable for earthquake-prone areas, under appropriate framing (Yang et al., 2022). Its inherent durability and resistance to corrosion — due to galvanization — contribute to its long-term reliability and minimal maintenance requirements.

The diverse capabilities offered by CFS are well known throughout the building industry, resulting in widespread adoption across various types of construction projects. As a suitable alternative to concrete or wood materials, it represents an efficient approach that contributes to cost-effective developments in both residential settings and more complex commercial facilities such as offices or factories (Dar et al., 2020). The easy-to-manipulate qualities promote fast installation possibilities, serving benefits concerning time reduction while reducing overall labor costs and simultaneously emphasizing financial savings.

One of its main applications is in light steel frame (LSF) construction, a technique that involves using thin sheets of galvanized steel to create load-bearing structural components for buildings. These components are typically formed into C-shaped or U-shaped sections and are assembled to create the framework of a structure. Such technique stands out particularly in renovation, retrofitting, and modular construction, being a key factor in the movement of panel construction — refers to the process in which walls or floors are manufactured in a factory and then transported to the construction site, where they are erected and connected to other panels.

To meet the desire to increase elements loading capacity, due to taller and taller buildings, a natural answer was to combine simple cross-sections. Thus, built-up cross-sections were created to enable bigger and more complex projects to be executed, providing the structural elements with higher torsional stiffness and larger spans, in other words, the strength of the group is higher than the sum of individual parts (S.-F. Nie et al., 2020) — regarding the moment of inertia increase —, being coined as “the second generation of CFS products”. Moreover,

individual cross-sections are usually monosymmetric, hence shear and gravity center do not coincide, but built-up cross-sections are symmetric (Craveiro et al., 2022b). Most of the times, the connection between sections is achieved with self-drilling screws, but it is possible with seam-welds too (Reyes and Guzmán, 2011).

There are some disadvantages though. Much like other kinds of steel, CFS is susceptible to corrosion, demanding proper coating and maintenance to ensure long-term durability, and to fire, calling for protective materials to retain its mechanical properties. Also, CFS design can be more complex due to its unique characteristics, requiring specialized expertise (Ranawaka and Mahendran, 2009). Lastly, compared to traditional methods, CFS may have higher initial material costs, though this can be offset by its efficiency during construction.

Despite these drawbacks, that fade in comparison to the number of advantages, CFS adoption seems to be a smart choice. It is favored for its high strength-to-weight ratio, enabling efficient material use and cost savings (Rinchen et al., 2019). Moreover, the design flexibility, eco-friendliness, and durability, make it a sustainable choice. Overall, CFS construction combines economic, environmental, and functional advantages for modern buildings.

1.2 Motivation

First and foremost, this thesis is philosophically motivated by the prospect of improving CFS design. The goal is to generate better understanding of built-up CFS columns — especially the composite action aspect —, and how it behaves when fire comes into the equation, thus leading to more precise ways to deal with these phenomena. It also focuses on questioning the present methodologies, because, as shown by Huang (Huang et al., 2021) and Ellobody (Ellobody and Young, 2005), Eurocode's predictions are usually over conservative. To improve these predictions, it would be valuable to incorporate the spacing between fasteners in built-up elements, and how it affects the overall load bearing capacity under fire.

Summarizing, this thesis seeks to shed light on said questions and to help filling some of the voids in this crescent field of study that is CFS structures.

1.3 Objectives

The objectives are:

- Evaluate the structural behavior of CFS columns;
- Analyze and compare the elements failure at ambient temperature, and fire conditions;
- Understand much does the spacing of the fasteners impact on the composite action between plates;

- Find the acceptable boundaries to the fastener's spacing values;
- Confront the parametric studies results to the existing Eurocode methodology;
- Examine the participation of local and global buckling in the collapse.

2 STATE OF THE ART

2.1 Fire Safety Engineering

The discipline of Fire Safety Engineering has a somewhat tragic history, that can be traced back to the middle of the 20th century. It gained traction as a field of study and practice after fire incidents such as the Cocoanut Grove fire in Boston in 1942 (Fig. 1a) and — in the Portuguese (Fig. 1b) context — the Chiado fire in 1988. These events highlighted the lack of good fire safety measures and led to the development of a systematic approach to understanding fire behavior, to mitigate its impact on buildings and the population. But it was not before the infamous 9/11 attack on the Twin Towers in New York City (Fig. 1c) that fire safety gained full relevance and rose to become the robust field of study that it is nowadays.

Figure 1 — Notable fire related incidents: a) Cocoanut Grove (Boston Globe@, 2019); b) Chiado (Sic Notícias@, 2018); c) Twin Towers (NBC News@, 2021)

Since then, it has advanced to become a vital aspect of buildings design — often being a key design factor for steel structures —, construction and risk assessment. Its importance to mitigating fire-related is indelible.

So much so that, besides design regulations, many countries have associations and councils to ensure proper safety. The most prominent are the National Fire Protection Association (NFPA) in the USA, the Institution of Fire Engineers (IFE) in the UK, the Fire Protection Association Australia (FPA Australia), the Vereinigung zur Förderung des Deutschen Brandschutzes (VFDB) in Germany, the Japan Fire Retardant Association (JFRA) and the Emirates Fire and Rescue Company (EFRC) in the UAE.

This field of study employs both passive and active protection methods to lessen the risk of having fires generating disproportionate damage or collapse. Passive measures prevent the spread of fire, and heat by incorporating fire-resistant materials, barriers, compartmentalization, and properly designed escape routes. *I.e.,* it works to provide safe evacuation routes for occupants by containing the fire within limited areas. Meanwhile, active measures use specific systems to actively detect, control, and suppress fires: alarm systems, sprinkler systems, smoke control systems, and emergency lighting. In other words, they aim to detect, and suppress fires at their early stages, creating conditions that promote safe evacuation and the effective response of firefighting personnel. But is not enough choosing one or the other. Even though each one reduces the level of risk, there must be a combination to provide acceptable levels of fire safety (Askaripoor, 2018).

This thesis focuses only on structural design under fire circumstances, but Fire Safety Engineering is much broader than that, encompassing areas such as fire protection systems, fire modeling, fire risk assessment, evacuation planning, and fire safety regulations, among others.

2.2 Cold-Formed Steel

The concept of cold-working steel — shaping and forming at low temperatures — has been present for centuries, but the use of CFS in buildings can be dated to the 1850s in both the USA and the UK. However, it was not until around 1940 that these elements were widely seen in the construction sector (Yu et al., 2020). That is because during the 1920s and the 1930s, significant advancements in the manufacturing process were made to better produce and understand the material's behavior, such as improving rolling techniques and equipment, standardization, improvements in connection methods and testing and research. But the catalyst for said advances was the rapid industrialization and urbanization of the period, that created a solid demand for cost-effective and versatile building materials.

With thicknesses varying between 0.378 mm and 6.35 mm, the diverse geometries of sections can be divided in two main types: individual structural framing members and panels and decks. The former representing a linear element, while the latter representing a planar element.

Regarding its manufacturing, there are three forming methods: cold roll forming, press brake operation and bending brake operation. Being the first the more common, it is a multi-step process. First, a suitable grade of steel coil or sheet is selected. The coil is loaded onto a decoiler, which unwinds it for further processing. The steel strip then goes through straightening rollers to remove any deformations. Then, the strip passes through a series of roll-forming stations, where it undergoes incremental shaping and bending to achieve the desired cross-sectional shape. Once formed, the profile is cut to the required length using a shear. If needed, holes or slots are punched into the profile for fastening or assembly purposes. The profile may undergo post-forming treatments such as surface coatings or treatments for enhanced durability. Quality control inspections are conducted throughout the production process to ensure dimensional accuracy and structural integrity. Finally, the finished profiles are packaged and prepared for shipping or storage, ready to be used in construction or manufacturing project (Yu et al., 2020). Some examples are found in Fig. 2.

Still according to Yu (Yu et al., 2020), the combination of the following factors result in cost savings and are the main advantages of CFS using:

- Lightness
- High strength and stiffness
- Ease of prefabrication and mass production
- Fast and easy erection and installation
- Substantial elimination of delays due to weather
- More accurate detailing
- Nonshrinking and noncreeping at ambient temperatures
- Formwork unneeded
- Termite proof and rot proof
- Uniform quality
- Economy in transportation and handling
- Noncombustibility
- Recyclable material

Figure 2 — Common CFS profiles (Wei-Wen et al., 2020)

2.3 Eurocodes

2.3.1 EN 1993-1-1:2005, EN 1993-1-3:2006 and EN 1993-1-5:2006

The EN 1993-1-1:2005 ("EN 1993-1-1, Eurocode 3: Design of steel structures — Part 1–1: General rules and rules for buildings," 2005) sets the ground rules to steel designing. One of its critical aspects is classifying cross-sections based on how easily local buckling could affect its resistance and rotation capacity. Generally, the classes 1 and 2 are those that can develop plastic resistance. Class 3 is the one that can reach the maximum elastic resistance, but local buckling hinders the development of plastic resistance. Lastly, class 4 is the one in which local buckling will occur before the stress at any compressed fiber could reach the yield stress. CFS elements usually fall into the latter, therefore are highly susceptible to this kind of phenomenon.

Regarding columns, in the sixth chapter — Ultimate Limit State — it is extracted that, beyond having a cross-section safely capable of bearing the applied load, an element under compression must resist the buckling effects of said load. This resistance is weighted by a reduction factor that takes into consideration the columns slenderness, it's elastic critical force for the relevant buckling mode and the inherit imperfections (through the buckling curves). For class 4 elements, the effective geometric properties must be used in this scope.

The EN 1993-1-3:2006 ("EN 1993-1-3, Eurocode 3: Design of steel structures — Part 1–3: General rules, supplementary rules for cold-formed members and sheeting," 2006) is the one

responsible for the specificities of cold-formed members, establishing its properties, tolerances, durability, analysis and uses. It sets how should torsional and flexural buckling be analyzed, even indicating what buckling curve to use.

The EN 1993-1-5:2006 ("EN 1993-1-5, Eurocode 3: Design of steel structures — Part 1–5: Plated structural elements," 2006) discusses the plated steel elements. It lays the ground rules to calculate the effective characteristics of class 4 cross-sections, that are constantly threatened by local buckling and shear lag.

Combining these three documents it is possible to calculate the resistance of CFS columns at ambient temperature, though the Effective Width Method (EWM), as done by Craveiro (Craveiro et al., 2022b), and detailed below.

For a column with a class 4 cross-section, subjected to compression only, the load bearing resistance ($N_{b,Rd}$, in Eq. (1)) depends on the effective area (A_{eff}), the steel yield strength (f_y) and the reduction coefficient (χ). The first component, effective area, is evaluated according to the EN 1993-1-3:2006, taking into account both distortional and local buckling stresses (clause 5.5 of the EN 1993-1-3:2006 for the first and clause 4.4 of the EN 1993-1-5:2006 for the latter). Thus, for a lipped channel, A_{eff} is found by Eq. (2), considering the effective plate length (b_{eff}, in Eq. (3)) obtained via the reduction factor for plate buckling (ρ, in Eq. (3)), and the effective thickness of the edge stiffener, by calculating the reduction factor for the distortional buckling (χ_d, in Eq. (2)). The effective section area, which consists of a reduction of the plates' width in compression, depends on elastic local buckling stress (Eq. (4)) and the thickness of the edge stiffeners and the distorted parts of the compression flanges, depend on elastic distortional buckling stress (Eq. (5)). The aforementioned reduction factor for plate buckling is achieved using the expressions in clause 4.4 of the EN 1993-1-5:2006. The effective areas were determined considering the individual shapes and then summed. The second component, yield strength, comes directly from the kind of steel used. Finally, the third component, reduction coefficient for the relevant buckling mode (χ), is calculated by Eq. (6), being φ an auxiliar coefficient reached through Eq. (7). The imperfection factor (α) comes from the Table 6.3 of the EN 1993-1-3:2006, which indicates that the appropriate buckling curve for built-up members is buckling curve *b* — Figure 6.4 of the EN 1993-1-1:2005 —, if f_{yb} is used.

$$N_{b,Rd} = \frac{\chi A_{eff} f_y}{\gamma_{M1}} \tag{1}$$

$$A_{eff} = t[h_{e1} + h_{e2} + 2b_{e1} + 2(b_{e2} + c_{e2})\chi_d] \tag{2}$$

$$b_{eff} = \rho b \tag{3}$$

$$\sigma_{cr} = \frac{k_\sigma \pi^2 E}{12(1-\upsilon^2)\left(\frac{b}{t}\right)^2} \tag{4}$$

$$\sigma_{cr,s} = \frac{2\sqrt{KEI_s}}{A_s} \tag{5}$$

$$\chi = \frac{1}{\varphi + \sqrt{\varphi^2 - \overline{\lambda}^2}} \tag{6}$$

$$\varphi = 0{,}5\left[1 + \alpha\left(\overline{\lambda} - 0.2\right) + \overline{\lambda}^2\right] \tag{7}$$

$$\overline{\lambda} = \sqrt{\frac{A_{eff} f_y}{N_{cr}}};\ N_{cr} = min\left\{N_{cr,F}, N_{cr,T}, N_{cr,FT}\right\} \tag{8}$$

$$N_{cr,F} = \frac{\pi^2 EI}{L_e^2} = \frac{\pi^2 EA}{\left(\frac{L_e}{r}\right)^2} \tag{9}$$

It is worth mentioning that the Eurocode does not have a specific methodology to consider the degree of connection between plates in a built-up CFS cross-section, only for hot rolled steel built-up cross-sections. Therefore, it is common practice between designers and researchers to assume perfect interaction based on what is provided by the Eurocode. This issue is particularly problematic, since interaction is one of the most important aspects of CFS design (Rasmussen et al., 2020).

2.3.2 EN 1993-1-2:2005

In the EN 1993-1-2:2005 ("EN 1993-1-2, Eurocode 3: Design of steel structures — Part 1–2: General rules - Structural fire design," 2005) the fire effects on steel structures is elaborated. The Eurocode adopts the methodology of reducing the load bearing capacity through the mechanical reduction factors, while reducing the acting load through the load reduction factor.

The procedure to verify a column fire design is thoroughly expressed below:

- It shall be verified that, during the exposure, the design effect of actions for the fire situation must not surpass the corresponding resistance.

$$E_{fi,d} \leq R_{fi,d,t} \tag{10}$$

- The effect of actions for the fire situation can be obtained from the corresponding effect of actions for a fundamental combination at normal temperature. As a conservative simplification, the reduction factor can be used as 0,65.

$$\eta_{fi} = \frac{G_k + \psi_{fi} Q_{k,1}}{\gamma_G G_k + \gamma_{Q,1} Q_{k,1}} \tag{11}$$

- For the resistance member of the inequation, the first step is to classify the cross-section, according to the Table 5.2 of the EN1993-1-1:2005, with the reduced value of ε. All built-up cross-sections studied are class 4, as show in the aforementioned ambient temperature article.
- For class 4 members under compression, the buckling resistance is given as a function of the temperature (Annex E of the EN 1993-1-2:2005).

$$N_{b,fi,\theta,Rd} = \frac{\chi_{fi,\theta} A_{eff} k_{y,\theta} f_y}{\gamma_{M,fi}} \tag{12}$$

- The reduction factor for flexural buckling in the fire design situation is taken as the lesser value between both bending axes.

$$\chi_{fi,\theta} = \frac{1}{\varphi_\theta + \sqrt{\varphi_\theta^2 + \overline{\lambda}_\theta^2}} \tag{13}$$

- With

$$\varphi_\theta = 0{,}5 \left[1 + \alpha \overline{\lambda}_\theta + \overline{\lambda}_\theta^2\right] \tag{14}$$

$$\alpha = 0{,}65 \sqrt{\frac{235}{f_y}} \tag{15}$$

- The non-dimensional slenderness for a given temperature is the non-dimensional slenderness at ambient temperature weighted by a temperature dependent ratio. This dependency is translated through the reduction factors displayed in the Table 3.1 of the EN 1993-1-2:2005.

$$\overline{\lambda}_\theta = \overline{\lambda} \sqrt{\frac{k_{y,\theta}}{k_{E,\theta}}} \tag{16}$$

Albeit being enough for cases when the end temperature is known, there are instances in which the critical temperature is not known. For the latter, an iterative procedure is needed: the first temperature is arbitrated as 20°C, then the $N_{b,fi,20,Rd}$ is calculated to assess the degree of

utilization. This enables the first attempt of calculating the critical temperature. From that moment on, the critical temperature is fed as the following iterations temperature until a desirable convergence is reached.

$$\mu_{0,\theta} = \frac{E_{fi,d}}{N_{b,fi,\theta,Rd}} \tag{17}$$

$$\theta_{a,cr} = 39{,}19 \ln\left[\frac{1}{0{,}9674\mu_{0,\theta}^{3{,}833}} - 1\right] + 482 \tag{18}$$

It is necessary to state that the Eurocode considers the temperature uniform along the element.

The EN 1993-1-2:2005 approach to class 4 cross-sections compression members subjected to fire is basic and overconservative (Huang et al., 2021), as seen in the recommendation to restrict the elements to a 350 ºC critical temperature. Nevertheless, for this level of temperature, the Table E.1 of the EN 1993-1-2:2005 shows that the reduction coefficient is 0.72, *i.e.*, the element is still in reasonable conditions to resist.

2.4 Literature review

2.4.1 Imperfections

Both geometric and material imperfections are inevitable. The former due to natural manufacturing factors, storage, and transportation and the latter due to impurities and material heterogeneity. In a FEA, these arch and wave shaped irregularities can physically be considered. First is necessary an LBA model to calculate the buckling deformed shape corresponding to the relevant modes, then this information will be used as input in another model — a GMNIA, for example —, multiplied by a coefficient. Said coefficient has been subject to many studies, according to the given situation (Table 1).

Table 1 — Studies on imperfections

Reference	*Coefficient*
(Dabaon et al., 2015) (Kherbouche and Megnounif, 2019)	$L/1100$ for global imperfection of columns with length up to 3000 mm; $0.005t$ for local imperfection, being t the profile's thickness.
(Craveiro, 2015)	$L/1000$ for global imperfection; $h/200$ for local imperfection.
(Meza et al., 2020a)	Laser sensor measured imperfections; maximum of $1.04\ mm$ (local) for a 1100 mm length column;
(Rahnavard et al., 2021)	Compared multiple coefficients to adhere to the most conservatives: the ones advocated by Craveiro.

Residual tensions are also somewhat related to the topic of imperfections but are not much relevant when talking about fire. That is because these tensions, which result from the profile's uneven cooling, end up levelling up when the element is submitted to fire and expansion.

2.4.2 Columns at ambient temperature

The state of the art on the topic of CFS columns can be observed in some of the following articles.

- Craveiro (Craveiro et al., 2022b) laid the foundation to the present study, by evaluating the behavior of closed built-up CFS columns under ambient temperature compression. Tests and numerical models were created to show that higher overlapping perimeter works against local buckling and that, when local buckling governs, the fastener spacing should be smaller than the local buckle half-wavelength. Finally, when comparing the results to existing analytical methods, the EWM fell behind DSMs modified slenderness ratio component;
- Georgieva (Georgieva et al., 2012) detailed the process of designing build-up CFS columns according to the AISI S100-2007 DSM;

- Rahnvard (Rahnavard et al., 2021) did numerical experimentation on CFS battened columns, finding out that fastened connected batten plates — with at least two rows of fasteners — showed higher axial load bearing capacity, in comparison to welded ones. Also concluded that three horizontal rows of fasteners is the optimal scenario, with no substantial impact generated when increasing this number;
- Nie (S.-F. Nie et al., 2020) tested thirty CFS elements with built-up closed cross-sections under concentric and eccentric compression. It was found that the screws spacing exerted less influence on the columns strength when the ends were fixed against torsion and restrained against wrapping;
- Veljkovic and Johansson (Veljkovic and Johansson, 2008) proved that, for thin-walled steel columns with open and partially closed cross-sections, both the EWM and the DSM give good predictions of the resistance;

2.4.3 Columns subjected to fire

One step beyond the ambient temperature analysis, the component of fire has not been vastly examined yet, but there are some remarkable studies, such as the following.

- Craveiro (Craveiro et al., 2014) delved into the open cross sections, performing 48 fire tests to conclude that the end support condition and initial applied load are paramount factors on their fire performance. Also verified that the temperature limitation of 350°C for class 4 cross-sections, present in the EN 1993-1-2:2005, is conservative for lipped channel columns, but realistic for most built-up I columns;
- Craveiro (Craveiro et al., 2016a) again turned to the fire behavior o CFS columns, but with closed built-up cross sections this time. A restrained elongation approach points to the importance of level of restraint — since a column like this cannot expand freely, incurring additional forces that can lead to premature collapse — and initial load applied. Once again, it is stated that the Eurocode's 350°C limit is very conservative;
- Laím (Laím et al., 2020) elaborated on the influence of intermediate and edge stiffeners on CFS columns subjected to fire, concluding that the global buckling mode was the predominant in failure and that double edge folds can lead to results 30% better than single edge folds, critical temperature wise. Finally, it is also said that existing analytical methods are incapable of performing realistic predictions on this complex topic;
- Laím (Laím et al., 2014) tackled the theme of CFS beams under fire circumstances with 36 tests to find out that even the smallest amount of axial restraint to the thermal elongation affects the critical temperature, with a decrease up to 30% when compared to the simply supported elements. Furthermore, it is noted that closed built-up cross-sections can be up to 50% more efficient than the open ones, regarding critical time.

- Huang (Huang et al., 2021) explored the behavior of cold-formed stainless steel RHS and SHS beam–columns subjected to fire, to discover that the Eurocode's EWM provides a much more conservative reading, compared to the DSM;
- Arrais (Arrais et al., 2021) examined and suggested adding a new β parameter to the design methodology for CFS lipped channels and Sigma channels under compression. Said parameter depend on the shape of the cross-section and would affect the imperfection factor (α) in fire scenario. The author advised using a value of 0.4 for sigma channels and 0.65 for lipped channels. Although built-up portions weren't specifically mentioned, built-up parts might be considered with the suggested methods by adjusting the β parameter;
- Yang (Yang et al., 2020) evaluated the fire response of sixteen unrestrained axially loaded CFS built-up box columns. The 2700 mm columns were observed to collapse under a combination of flexural and local buckling and regardless of the heating rate, load ratio, or temperature distribution patterns along the height, the specimens' failure zones were always where the temperature was the highest. He also concluded that when the slower heating rate was used, creep was seen in the experiments, which had a maximum impact of 8% on the member critical temperatures and that creep deformations were found to be more pronounced when lower load ratios were used, this was due to a longer exposure period and a higher temperature involving the specimen;
- Yang (Yang et al., 2022) followed his previous work by studying the fire response of six restrained axially loaded CFS built-up box columns. The still 2700 mm columns were also brought to collapse by a mix of local and global buckling at elevated temperatures. He concluded that the most important factors to the columns behavior are the axial restraining stiffness — similarly to what Laim (Laím et al., 2014) observed with beams — and the load ratio, since increasing one or both of them generates a higher internal force at the same temperature. In the numerical aspect, he spoke about the input data's applicability, focusing mostly on mechanical and thermal qualities. Researchers generally believe that the data supplied in current design standards such the EN 1993-1-2:2005 is inaccurate, because the reduction factor adopted are higher than the experimental ones (Craveiro et al., 2016b);
- Possidente (Possidente et al., 2020) carried out 23500 parametrical tests to check whether the EN 1993-1-2:2005 buckling curve provided accurate and safe predictions of compressed members subjected to fire, especially those prone to flexural-torsional buckling. He found that the regulation does not offer well-suited results, because the χ_{fi} is overestimated, and the predictions for stocky columns was very conservative. He then proposed a better calibrated curve, with a plateau in the beginning — for the stocky columns —, even including the possibility of slenderness modification to further improve the new methodology.

2.4.4 Miscellaneous

Lastly, there are other research that are not directly connected to the main theme of this study but can aggregate some context and value.

- Phan (Phan et al., 2020) conducted an optimization study leveraged by genetic algorithms on portal frames, under the Eurocodes methodology. Two instances of optimization — of the element and structural — were used to show that optimized frameworks could save up to 20% in material and present 84% higher ultimate capacity;
- Rasmussen (Rasmussen et al., 2020) studied CFS with built-up cross-sections under flexion and torsion to conclude that the degree of composite action is paramount to the design, being the load bearing capacity as high as the degree of connection;
- Ellobody and Young (Ellobody and Young, 2005) elaborated on how the design rules in the American, Australian/New Zealand and European specifications are generally conservative for cold-formed high strength stainless steel square and rectangular hollow section columns, but unconservative for some of the short columns.

2.5 Gaps to fill

Being a topic that needs further exploration, this thesis aggregates another set of cross-sections and columns configurations to the CFS built-up cross-sections columns subjected to fire literature. It also works to provide more experiments to broaden the observation pool of tested specimens, while exercising once again the development of finite element models.

However, the biggest impact this thesis seeks to generate is to build knowledge regarding the impact of spacing between plates. Said factor is extremely important to the composite action of the built-up cross-section, so understanding it is key to develop better and more robust design methodologies on future regulations, such as the Eurocode.

3 METHODOLOGY

3.1 Buckling tests

The study to assess the load capacity of the built-up CFS columns at ambient temperature was carried previously by Craveiro (Craveiro et al., 2022b), laying the foundation to the subsequent fire resistance tests and the present numerical analysis of these latter tests. The intent was for the short columns to fail predominantly by sectional buckling — local and/or distortional — of the individual profiles between connectors and the experimental procedure is detailed below.

3.1.1 Geometry of the built-up cross-sections

Commercially available cold-formed steel individual shapes, such as C, U, and Σ-shaped, made up the examined built-up members. With a nominal yield strength of 280 MPa and a nominal ultimate strength of 360 MPa, it was used S280GD+Z structural steel with a zinc coating (0.04 mm-275 g/m^2) to construct the profiles. Nominal dimensions for the C channel are 150 x 43 x 15 mm, 153 x 43 mm for the U channel, and 150 x 43 x 15 mm for the Σ channel, with 1.5 mm thick plates, as indicated in Fig. 3 and Table 2.

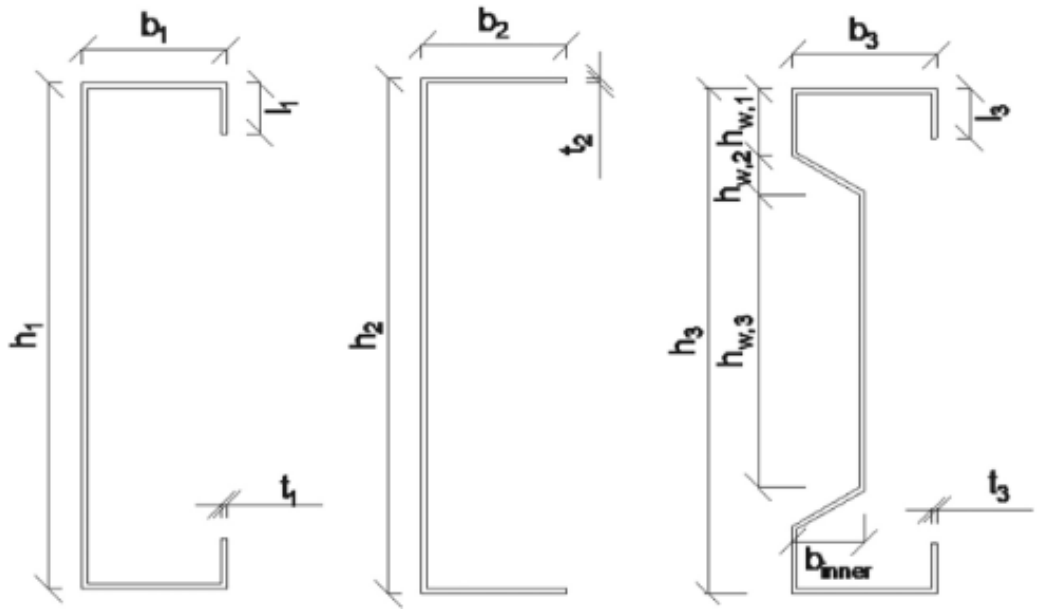

Figure 3 — Simple cross-sections used (Craveiro et al., 2022b)

Table 2 — Average measured dimensions for the individual shapes (Craveiro et al., 2022b)

C	b_1 *(mm)*	h_1 *(mm)*	I_1 *(mm)*	t_1 *(mm)*				
	42,96	149,94	15,16	1,499				
U	b_2 *(mm)*	h_2 *(mm)*	t_2 *(mm)*					
	153,08	43,06	1,504					
Σ	b_3 *(mm)*	b_{inner} *(mm)*	h_3 *(mm)*	$h_{w,1}$ *(mm)*	$h_{w,2}$ *(mm)*	$h_{w,3}$ *(mm)*	I_3 *(mm)*	t_3 *(mm)*
	43,03	19,99	150,16	20,3	12,3	85,66	15,4	1,498

These profiles were combined to form rectangular and square built-up members, with double symmetry, as shown in Fig. 4. Each element had a length of 1050 mm, and 6.3 mm-diameter fasteners were used to connect the plates. The columns geometry is detailed in Fig. 4 and Table 3, while the fasteners spacing that was adopted is illustrated in Fig. 5. At each end, endplates were spot welded, safeguarding a 50 mm zone. Hence, the chosen spacing can be interpreted as a fourth of the following: the column's length subtracted by the 50 mm zone at each end. This value was selected based on data from the literature — similarly to Meza (Meza et al., 2020b), and Nie (S. Nie et al., 2020) —, current usage, and preliminary numerical modeling (Craveiro et al., 2022b).

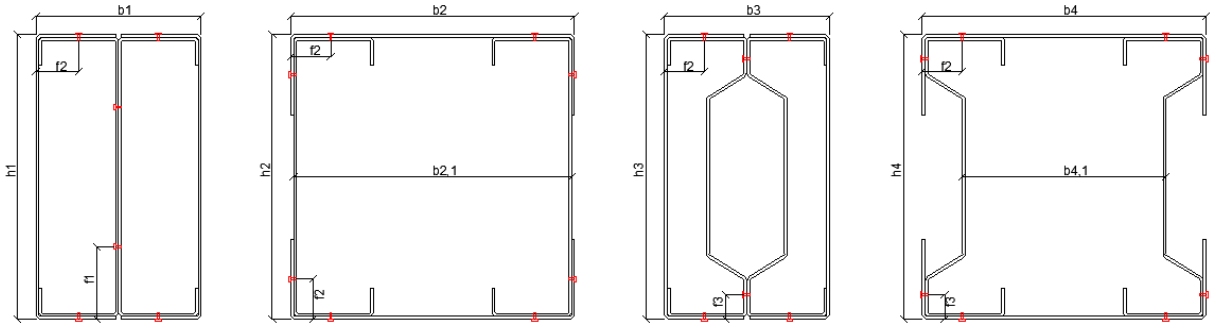

Figure 4 — Built-up cross-sections studied

Table 3 — Details of the fabricated specimens (Craveiro et al., 2022b)

Column configuration	*Length (mm)*	*Gross area (mm²)*	*CFS profiles*			*Fasteners distance (mm)*			*Fasteners spacing (mm)*
			C	*U*	*Σ*	*f1*	*f2*	*f3*	
R-2C+2U	1050	1453	2	2	—	39	23	—	237.5
S-2C+2U	1050	1453	2	2	—	—	21.5	—	237.5
R-2Σ+2U	1050	1531	—	2	2	—	21.5	11.5	237.5
S-2Σ+2U	1050	1531	—	2	2	—	21.5	11.5	237.5

Where *f1*, *f2* and *f3* can be identified in Fig. 4.

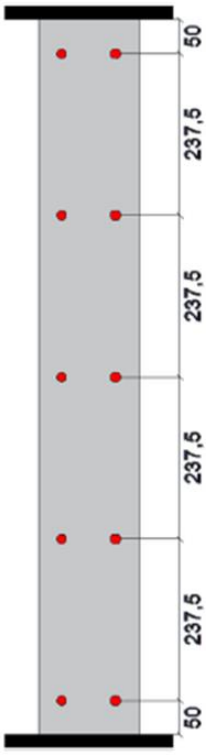

Figure 5 — Fasteners configuration used in the tests (Craveiro et al., 2022b)

3.1.2 Experimental tests

To evaluate the structural behavior, buckling loads, and failure modes of closed built-up CFS, twelve quasi-static compression experiments, with controlled displacement until failure, were performed, three for each one of the four configurations. Hence, ensuring statistical validation to the results.

3.1.3 Mechanical and thermal properties

Mechanical tests on flat and corner coupons were conducted (Table 4), according to the ISO 6892-1 (International Organization for Standardization, 2006), to access the influence of the cold-forming process on these properties. The results show that an increase of 23.8% on the yield strength, and 5.9% on the ultimate strength.

Table 4 — Mechanical Properties of the S280Gd+Z (buckling tests) (Craveiro et al., 2022b)

	$\bar{E}_s$ *(GPa)*	$\bar{f}_y$ *(MPa)*	$\bar{f}_u$ *(MPa)*	$\bar{f}_p$ *(MPa)*	$\bar{\varepsilon}$ *(%)*
Flat	204.7	305.9	426.1	214.5	22.9
Corner	205.1	378.6	451.0	241.9	13.2

3.1.4 Fastener behavior

The composite action is not achieved if the fasteners are not properly assigned. So, two shear tests were performed to characterize the connector's stiffness and resistance. Both results came in good agreement, proving that the self-drilling screws would not be put the columns' tests in question.

3.1.5 Imperfection measurements

The elements imperfections were measured using a 3D scanning technique, with the Creaform Metrascan 750 Elite — accuracy of the equipment is of up to 0.03 mm with a resolution of up to 0.05 mm — and the data treatment followed the equation and strategy adopted by Xiong (Xiong et al., 2016) and Le (Le et al., 2020). The highest imperfection measured was 0.82 mm for the R-2C+2U built-up member, 1.49 mm for the S-2C+2U, 0.52 mm for the R-2Σ+2U, and lastly 1.89 mm for the S-2Σ+2U built-up member (Fig. 6).

$$D_{ai} = d_i - \frac{[(30-i)\times d_1 + (i-1)\times d_{30}]}{29}, i \in [1,\dots,30] \quad (19)$$

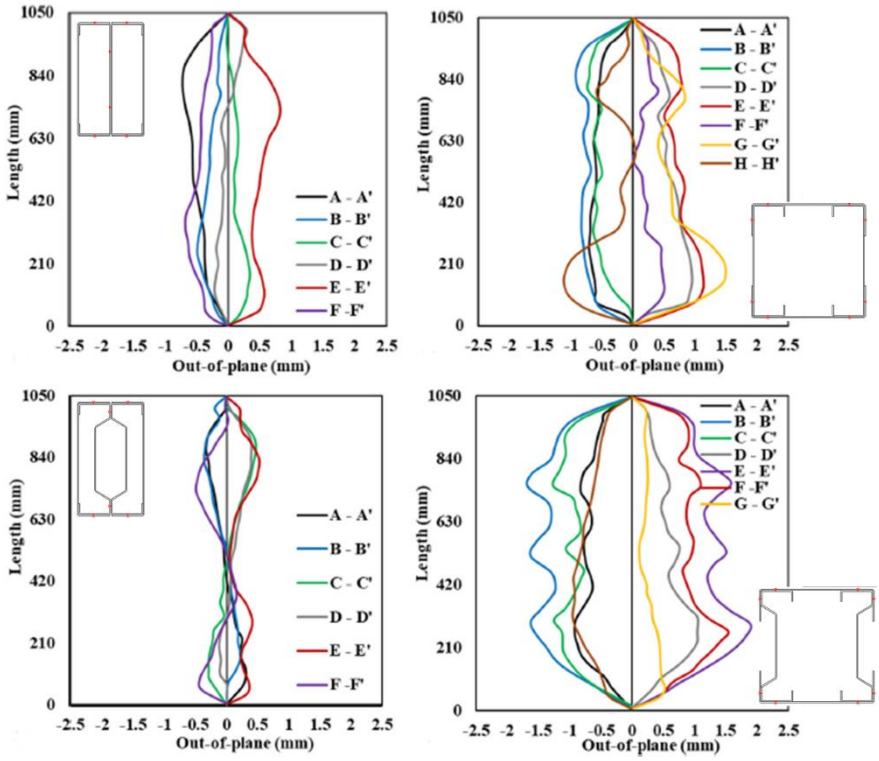

Figure 6 — Imperfections measured in the fabricated specimens (Craveiro et al., 2022b)

3.1.6 Test set-up and instrumentation

The compressive tests were performed by a hydraulic machine, with 5000 kN capacity. The experiments were terminated when the load was reduced by at least 50%. Compressive loading was administered under displacement control at a constant rate of 0.01 mm/s.

3.2 Fire resistance tests

As mentioned at the beginning of Subchapter 3.1, the fire resistance tests come as successor to the buckling tests, in the sense of evaluating the columns behavior, then how they how they fare in elevated temperatures. Much of the subjects and procedures are shared between them.

3.2.1 Geometry of the built-up cross-sections

The chosen shapes were the same as the ones presented at Subchapter 3.1.1: C (150 x 43 x 15 mm), U (150 x 43 mm) and Σ (150 x 43 x 15 mm) — Table 2 for the measurements. All of

them made with the aforementioned S280GD+Z hot-dip galvanized with zinc (zinc coating of 0.04 mm – 275 g/m2) structural steel, presenting a 280 MPa nominal yield strength and a 360 MPa ultimate strength.

Regarding the configuration, it was also adopted two rectangular and two square built-up cross sections, in 1050 mm columns — to focus on sectional buckling and to match the physical limitations of the furnace. The square ones were designed to fail by local plate buckling, considering that the total length is larger than three times the length of the web and smaller than 20 times the least radius of gyration (Ziemian, 2010). Whereas for the rectangular ones, some interaction between local and global buckling may occur. The details can be seen at Table 3.

The fasteners spacing is alike the one depicted in Fig. 5, with 6.3 mm diameter connectors. The disposition at the cross-section is presented at Fig. 4 and Table 2.

3.2.2 Mechanical and thermal properties

Once again using coupon specimens, only the ambient temperature of the S280GD+Z were determined. The elevated temperature properties came from a previous study of Craveiro (Craveiro et al., 2016b) on the same steel grade. The resultant stress-strain curves for the ambient temperature tests are depicted in Graph 1, while the mechanical properties are presented in Table 5 — average yield stress 304.4 MPa and Young's modulus 201.9 GPa. Lastly, the reduction factors reported by Craveiro (Craveiro et al., 2016b) for this type of structural steel are displayed in Graph 2 — regarding class 4 cross-sections.

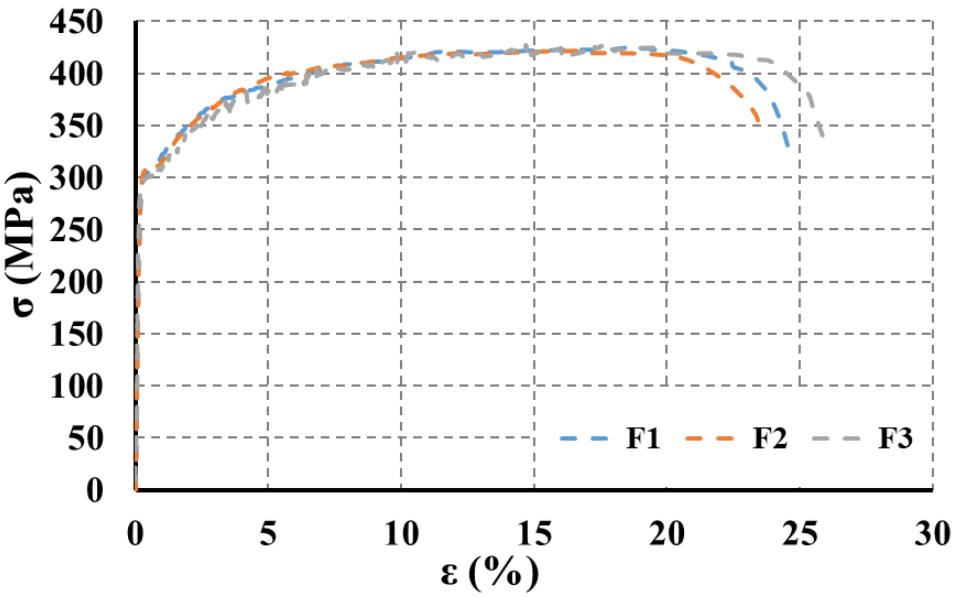

Graph 1 — Mechanical properties of the coupon specimens (Craveiro et al., 2022b)

Table 5 — Mechanical Properties of the S280Gd+Z (fire resistance tests) (Craveiro et al., 2022a)

Test	E_s *(GPa)*	$\bar{E}_s$ *(GPa)*	f_y *(MPa)*	$\bar{f}_y$ *(MPa)*	f_u *(MPa)*	$\bar{f}_u$ *(MPa)*	f_p *(MPa)*	$\bar{f}_p$ *(MPa)*	ε *(%)*	$\bar{\varepsilon}$ *(%)*
F1	203.4		305.03		425.1		208.28		24.52	
F2	205.4	201.9	308.10	304.4	421.8	424.8	210.97	214.5	23.43	24.6
F3	197.1		299.97		427.6		218.24		25.95	

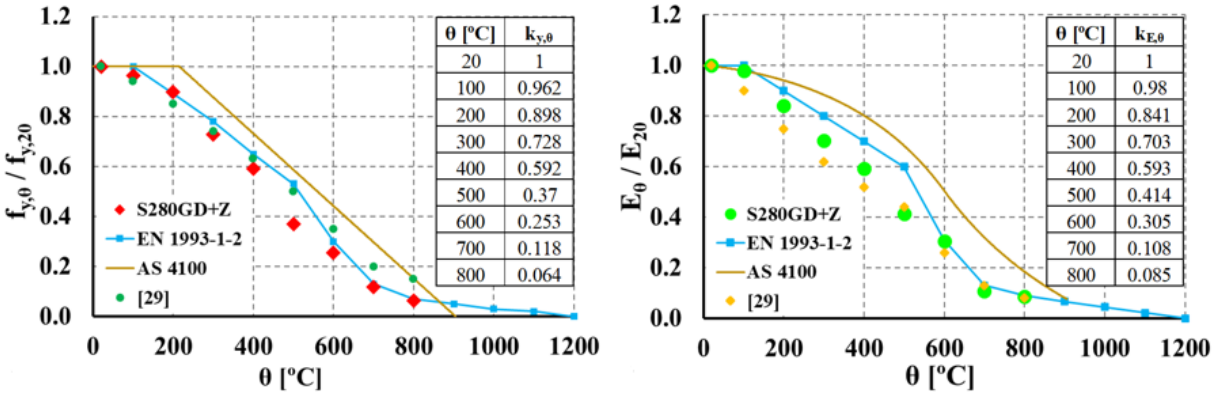

Graph 2 — Mechanical properties calculated at elevated temperatures (Craveiro et al., 2016b)

3.2.3 Imperfection measurements

The imperfections were, again, measured with the Creaform Metrascan 750 Elite 3D scanner. It was maintained the approach of data treatment with Eq. (19) and the procedures described by Xiong (Xiong et al., 2016) and Le (Le et al., 2020). The maximum measurements were used to calibrate the numerical model and are 0.825 mm for the R-2C+2U, 1.288 mm for the S-2C+2U, 0.704 for the R-2Σ+2U, and 1.335 mm for the S-2Σ+2U.

3.2.4 Test set-up and instrumentation

The set-up (Fig. 7) was composed a large reaction frame (1), in which a hydraulic jack (4) was fixed and a secondary 3D surrounding frame (2) where the load cells (5), and boundary condition devices — tailored to prevent premature collapse of the columns ends — were

positioned. The columns (3) were fixed at both ends. It is noteworthy that the built-up CFS can expand freely during heating without producing additional axial tensions. 40% of the buckling load obtained in the experimental tests at ambient temperature — Subchapter 3.1 (Craveiro et al., 2022b) — was applied as service load (Table 6).

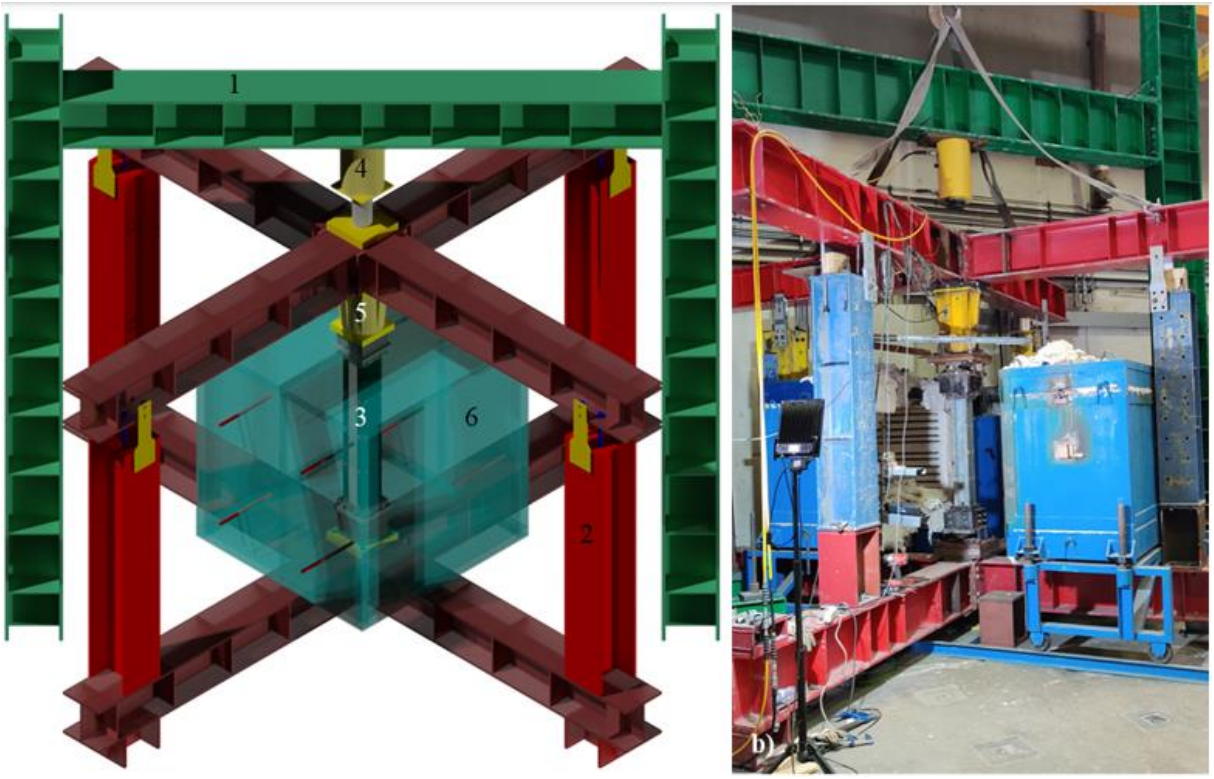

Figure 7 — Fire test set-up

Table 6 — Experimental results at ambient temperature and corresponding serviceability load used in the fire resistance test (Craveiro et al., 2022a)

Test	$P_{u,Test}$ *(kN)*	$\bar{P}_{u,Test}$ *(kN)*	$0.4\bar{P}_{u,Test}$ *(kN)*	*Test*	$P_{u,Test}$ *(kN)*	$\bar{P}_{u,Test}$ *(kN)*	$0.4\bar{P}_{u,Test}$ *(kN)*
R-2C+2U_1	259.60	256.37	102.55	*S-2C+2U_1*	232.78	240.89	96.36
R-2C+2U_2	267.00			*S-2C+2U_2*	248.00		
R-2C+2U_3	242.50			*S-2C+2U_3*	241.89		
R-2 Σ +2U_1	320.70	311.07	124.43	*S-2 Σ +2U_1*	320.30	309.20	123.68
R-2 Σ +2U_2	310.20			*S-2 Σ +2U_2*	295.40		
R-2 Σ +2U_3	302.30			*S-2 Σ +2U_3*	311.90		

To conduct the test, the prescribed serviceability load was applied to each of the configurations. Force control was used while applying the intended load. The electric furnace was turned on after the predetermined load had been met. Although the furnace (6) was initially configured to replicate the ISO 834 fire curve (International Organization for Standardization, 2014), some variations in temperature evolution could be seen because of the initial thermal inertia. The built-up CFS column would expand freely during the heating stage while keeping the initial service load constant, up until a point when it was no longer able to support the applied load due to the substantial degradation of mechanical properties of the cold-formed steel with increasing temperature.

Loads, displacements, and temperatures were monitored in every test. The first through the hydraulic jack. The second through linear variable differential transducers (LVDTs), connected to the specimens through nickel-chromium alloy wires. The ones installed at mid-height measured the horizontal displacements, while the ones at the extremities measured the vertical displacements, throughout the axial shortening – axial elongation – axial shortening path. The

third one through thermocouples. Type K rod thermocouples were positioned along the height of the furnace to measure the temperature in the chamber. Type K thermocouples were welded to the surface of the CFS profiles at various points along the height of the column and at the cross-sectional level to measure the temperature of the steel. To track the temperature evolution of the gas inside the tubular built-up columns, a second thermocouple was installed at mid-height in the void of the tubular built-up sections.

3.3 Numerical modelling

Numerical models were used in two occasions: to reproduce the physical results observed in the compression tests — calibration —, and to extrapolate the tested conditions through the variation of other parameters — parametrization. The former employs the real material properties — obtained by stress-strain curves, for example — on the software, the ones which were tested or validated by other studies. In this study, these properties were indeed tested, for the ambient temperature, and then reliable studies were utilized to access them at elevated temperatures, as mentioned at Subchapter 3.2.2. The latter employs nominal material properties on the software — indicated by regulations, such as the Eurocode. In that way, the ground is set to compare the numerical results to the Eurocode's calculation methods. The software of choice to create the numerical models was Abaqus, version 2021 ("Abaqus Analysis User's Guide," 2017).

The calibration models — done beforehand by Craveiro (Craveiro et al., 2022a) — were made for each one of the columns configurations tested and they could successfully mimic the specimens (Graph 3).

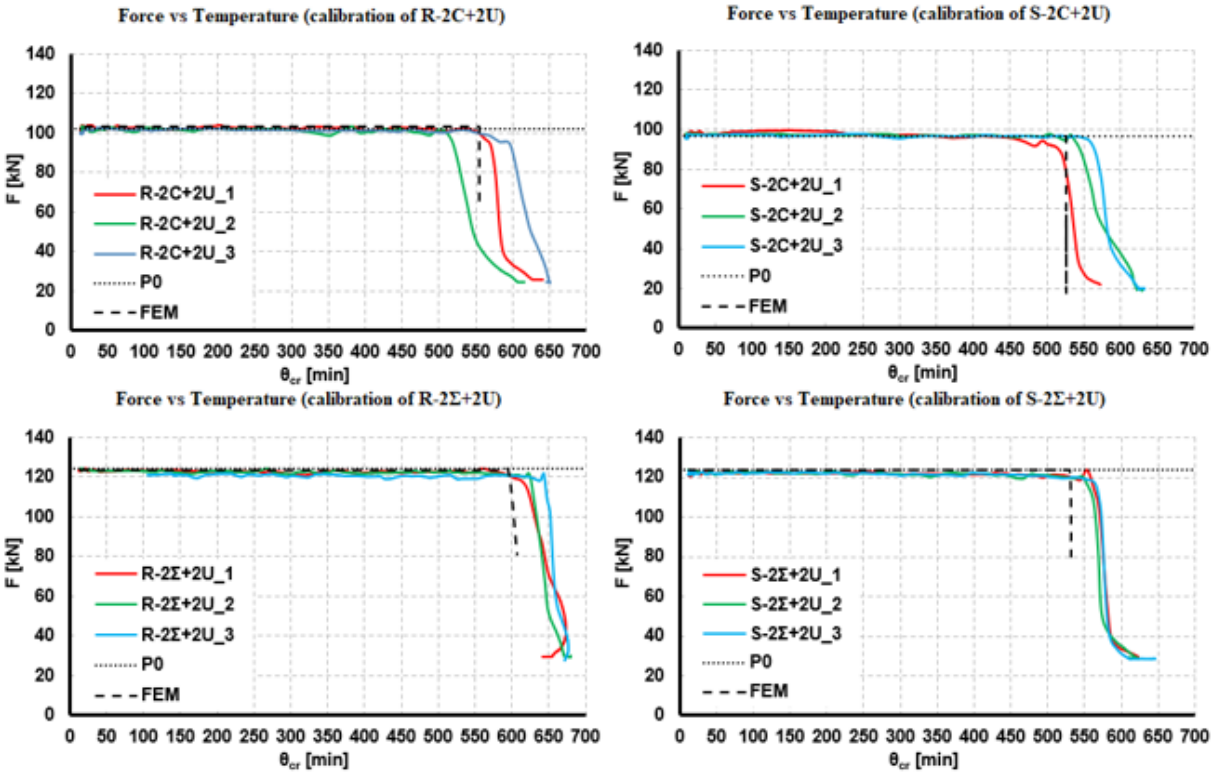

Graph 3 — Calibration of the numerical models (Craveiro et al., 2022a)

As can be seen in Graph 3, the concordance between the critical temperature observed physically and virtually is accurate, mainly when looking at built-up cross sections with C channels instead of Σ ones.

Eighty fire parametric tests were conducted in Abaqus, according to the matrix of parameters in Table7.

Table 7 — Adopted parameters to the parametric tests

Parameters	*Cross-section*	*Column length*	*Fasteners' spacing*		*Load level*
			1050 mm columns	*3000 mm columns*	
Cases	R-2C+2U S-2C+2U R-2Σ+2U S-2Σ+2U	1050 mm 3000mm	0,00 mm 118,75 mm 190,00 mm 237,50 mm 475,00 mm	0,00 mm 145,00 mm 290,00 mm 580,00 mm 1450,00 mm	30% $N_{b,Rd,FEM}$ 50% $N_{b,Rd,FEM}$

The parameters' choosing process was the following:

The present parametric cross-sections come from the experimental campaign.

The first length — 1050 mm — comes naturally from the experiments. The second length — 3000 mm — was selected to provide an increased slenderness to the columns, enabling global buckling modes to be seen more easily.

The spacings were chosen to be a reasonable fraction of the available length — *i.e.*, the column's length discounted by the 50 mm margin on both ends, as seen in figure 5. For example, a fourth, a fifth, an eighth, and so on.

Four spacing values were then selected from the following range: the cross-section's local buckle half-wavelength (Craveiro et al., 2022b) and half of the available length. The 0,00 mm spacing represents a perfect connection and was adopted to offer perspective, and ground of comparison to the Eurocodes, since it is the norm's base of assumption.

The load levels were chosen based on a low and a medium degree of utilization, being common practice, as seen in Laím's studies ((Laím et al., 2014), (Laím et al., 2020)) and Craveiro's (Craveiro et al., 2014), for instance.

The properties adopted in both calibration and parametrization are described below, as well as the detailed model's creation step-by-step.

The models are somewhat sequential, and one begins as a copy of the previous. It is not only beneficial to the time disposed, but mandatory to maintain a certain mesh, for when an analysis takes the result of another as input.

Figure 8 depicts an example of one specimen.

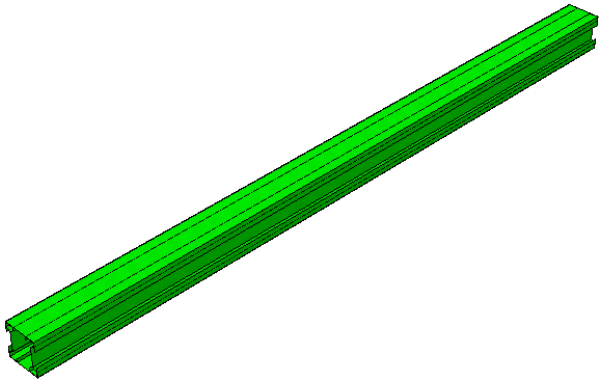

Figure 8 — Undeformed column example

3.3.1 Ambient temperature models

Only by knowing the column's bearing resistance at ambient temperature is possible to load them correctly under fire circumstances. So, each of the 80 columns subjected to fire simulation had the respective ambient temperature model.

To access the maximum compression force that an element withstands, two analyses are needed in the model: a Linear Buckling Analysis, and a Geometrically and Materially Nonlinear Analysis with Imperfections Included (GMNIA).

3.3.1.1 LBA

This analysis is the origin of the following ones. Based on the mesh created at the LBA, the other analyses will take shape by altering some components.

First, the column geometry is defined. Two parts were created through planar extrusion, one representing the lipped channel (C-shaped) and the other representing the plain channel (U-shaped). Furthermore, the datum planes were added to allow for partitions. These partitions help to define which surfaces are in contact and the placement of the fasteners.

The second phase is creating the material. The desired steel properties for this analysis are the density and the elastic properties (Young's Modulus and Poisson's Ratio), as shown in Table 8.

Table 8 — Mechanical properties of the LBA model

	Calibration	*Parametric*
Density [kg/m^3]	7850 (EN1993-1-2:2005)	
E [N/m^2]	204 000 000 000 (Modeled after the specimens' mechanical tested properties at ambient temperature: Subchapter 3.1.3)	210 000 000 000 (EN1993-1-1:2005)
v	0.3 (EN1993-1-1:2005)	

Still regarding the material is necessary to designate a shell homogenous section, with the corresponding 1.5 mm thickness, and assign it to both created parts.

The third phase is assembling the parts together, according to the type of built-up cross-section.

The fourth phase is creating the step, which is a buckle step, with number enough eigenvalues requested to observe every relevant buckling mode. Also defining the desired outputs, which is only the deformation (by default).

The fifth phase is in the domain of interactions. For starters, it is necessary to set-up the interaction properties, with the Normal and Tangential Behaviors. For the latter, it is used a 0.3 friction coefficient (Craveiro et al., 2022b), under a penalty friction formulation. Then an interaction was created, to represent the contact between adjacent plates. It was mostly used a general contact type, and a surface-to-surface contact type only for cases with difficult convergence. Must be noted that, this interaction is not necessary when the fastener's spacing is null.

Still under the Interaction tab, the constraints are coupling ones for the supports — being the master a reference point in the center of the cross-section and the slaves the surrounding edges of the same cross section — and ties between channels, when the spacing is null. The connectors must be determined too if there are fasteners. Beam is the connectors' type, with discrete 3.15

mm diameter fasteners. They are set in place through attachment points along the column's length and attachment lines indicating which surfaces to connect.

The sixth phase is creating a unitary load applied to the top of the element and the boundary conditions. Those are pinned, but with torsion restriction, to exclude torsion deformation modes.

The seventh phase is meshing the parts. A global 10 mm structured mesh was used, with shell S4R finite elements. A sensibility study was conducted between the 10 mm mesh and a 5 mm one. The difference was little — 1% in the $N_{b,Rd}$ — enough to conclude that the bigger mesh could be used, which brought time and computational advantages.

The eight phase is editing the keywords, asking for a file to be generated with the deformations of all modes.

The nineth, and final, phase is creating the respective job and submitting it to be run.

3.3.1.2 GMNIA (ambient temperature)

As a copy of the LBA, there are only a few changes to be made at this analysis.

The first change is in the materials tab, adding the plastic property to the existing density and elasticity. This was done following the trilinear plasticity behavior (Table 9) presented by Laím (Laím, 2013), who used a gradual yielding model of the steel starting at f_p, then to 87.5% f_y, to f_y, and finally to f_u. The stress-strain curve was set through these fractions of the yield strength and through four slopes that were percentages of the elastic modulus: 38, 10 and 5% of E.

Table 9 — Plastic properties of the GMNIA (ambient temperature) model

	Calibration	*Parametric*
Plasticity	Trilinear model (Laím, 2013)	Trilinear model (Laím, 2013)

The second change is the step, now adopting a general static step, with geometric nonlinearity. And requesting another set of outputs: deformation, reaction force, stress, Mises equivalent stress, plastic strain, and equivalent plastic strain.

The third is change is that there is no load, because this analysis is with controlled displacement. So, a displacement is added to the top support, forcing the column to show its maximum resistance.

The fourth and final change is in the keywords. Deleting the previous added command, regarding the deformed shape file, and adding a little script to import the LBA displacements and rotations as imperfections. These imperfections are pondered by the coefficients mentioned the subchapter 2.4.1. The multiplication factors used were the ones described in Table 10.

Table 10 — Imperfections of the GMNIA (ambient temperature) model

	Calibration and Parametrization	
	Local	*Global*
R-2C+2U	0.82 mm (Measured: Subchapter 3.1.5)	L/1000 (Craveiro, 2015), (Rahnavard et al., 2021)
S-2C+2U	1.49 mm (Measured: Subchapter 3.1.5)	
R-2Σ+2U	0.52 mm (Measured: Subchapter 3.1.5)	L/1000 (Craveiro, 2015), (Rahnavard et al., 2021)
S-2Σ+2U	1.89 mm (Measured: Subchapter 3.1.5)	

The buckling modes were selected to represent de deformation in each type of channel and the global deformation, and the deformed configuration of a model tested in ambient temperature is shown in Fig. 9.

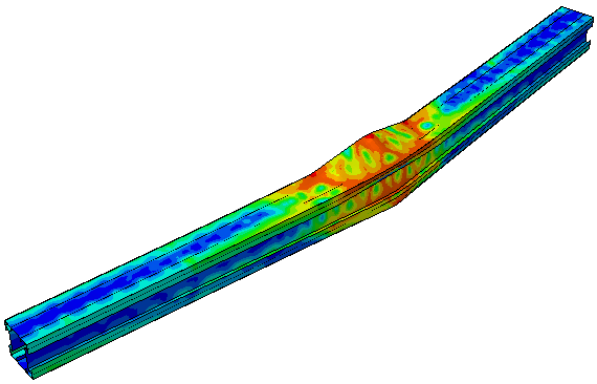

Figure 9 — Column after ambient temperature compression

3.3.2 Fire scenario models

Knowing the column's load bearing resistance, enables the development of the models that simulate the fire scenario.

To access the time and temperature that each one of the 80 columns can withstand three analyses are needed in the model: a Linear Buckling Analysis, a Heat Transfer Analysis, and a Geometrically and Materially Nonlinear Analysis with Imperfections Included.

3.3.2.1 LBA

This is the same LBA as the one created for the ambient temperature.

3.3.2.2 HT

As a copy of the LBA, there are only a few changes to be made at this analysis.

The first change is in the materials tab, removing the mechanical properties and adding the thermal properties — conductivity and specific heat (Table 11) — to the existing density. These thermal properties are the ones taken from the EN 1993-1-2:2005, clause 3.4 and they vary with temperature.

Table 11 — Thermal properties of the HT model

	Calibration	*Parametric*
Conductivity	Modeled after the specimens' thermal results: Subchapter 4.1	EN 1993-1-2:2005 clause 3.4
Specific heat		

The second change is the step, now adopting a transient heat transfer step, with a 20°C limitation of temperature change per increment, to guarantee a smooth temperature evolution. And requesting another set of outputs (by default): nodal temperature, heat flux vector, and reaction fluxes.

The third change is in the interaction tab. For starters, creating an amplitude that represents the ISO 834 curve (International Organization for Standardization, 2014), to simulate the temperature increase with time. Afterwards changing the interaction properties, adding the thermal conductance, and removing the mechanical properties (Table 12). To conclude the

alterations in this tab, it is still needed to delete the interaction related to mechanical aspect of contact and adding an interaction — surface-to-surface — related to the thermal conductivity aspect of contact. And to add the interactions that represent surface radiation — surface radiation — and convection — surface film condition. In the calibration study, the thermal properties were applied differently in the element, since the intent was to reproduce what was observed experimentally. But in the parametric study, the objective was to simulate a uniform temperature along the member, as the Eurocode considers, so these thermal interactions are applied equally to every plate. It is worth noting that the coupling restraints at the edges must be removed.

Table 12 — Thermal interaction properties of the HT model

	Calibration (Craveiro et al., 2022a)	*Parametric* (EN 1993-1-2:2005)
Thermal conductance [W/m^{2}K]	7000	2000
Film coefficient [W/m^{2}K]	15	25
Emissivity	0.16	0.35

The fourth change is removing all mechanical loads and supports. Also adding a predefined temperature field, homogenous, to indicate the initial temperature (20°C).

The fifth alteration is in the mesh tab, changing the element type to heat transfer DS4 elements, but not changing the mesh itself.

The sixth and final change is setting the attributes: absolute zero temperature and Stefan-Boltzmann constant (Table 13).

Table 13 — Attributes of the HT model

	Calibration	*Parametric*
Absolute zero (0 K) [°C]	-273.15 (Young and Freedman, 2008)	
Stefan-Boltzmann constant (σ) [W/m²K⁴]	$5.67x10^{-8}$ (EN 1993-1-2:2005)	

3.3.2.3 GMNIA (fire)

As a copy of the LBA, there are only a few changes to be made at this analysis.

The first change is in the materials tab. Maintaining the density, it is required to add the elasticity, the plasticity, and the expansion, all of which are temperature dependent. To get from the ambient temperature elasticity and plasticity — already covered at the GMNIA (ambient temperature) — to the temperature dependent ones, it is a matter of reduction factors. It was chosen to use the factors proposed by Craveiro (Craveiro et al., 2016b), since it is specific for the S280, instead of using the general ones present in EN 1993-1-2:2005 (Table 14). The expansion also must be added (Table 15).

Table 14 — Reduction factors for elevated temperatures

	(Craveiro et al., 2016b) *(Used both in calibration and parametric)*		*EN 1993-1-2:2005*	
	$f_{y,\theta}/f_{y,20}$ *(0.20% strain)*	E_θ/E_{20}	$f_{y,\theta}/f_{y,20}$	E_θ/E_{20}
20°C	1	1	1	1
100°C	0.962	0.980	1	1
200°C	0.898	0.841	1	0.900
300°C	0.728	0.703	1	0.800
400°C	0.592	0.593	1	0.700
500°C	0.370	0.414	0.780	0.600
600°C	0.253	0.305	0.470	0.310
700°C	0.118	0.108	0.230	0.130
800°C	0.064	0.085	0.110	0.090

Table 15 — Expansion property of the GMNIA (fire) model

	Calibration	*Parametric*
Expansion	Modeled after the specimens' thermal results: Subchapter 4.1	EN 1993-1-2:2005 clause 3.4

The second change is creating new steps. Using a general static step to load up the column, and an implicit dynamic step, which is more robust, therefore takes a toll on the computational processing, to heat up the loaded element. Both with active geometric nonlinearity. The outputs

asked for the pair: deformation, reaction force, stress, Mises equivalent stress, plastic strain, equivalent plastic strain, nodal temperature, and element temperature.

The third change is in the load tab. Now, the previous unitary load must be substituted by a percentage — 30% or 50% — of the column's bearing resistance at ambient temperature (calculated with the numerical models at ambient temperature). The geometrical placement is still in the top support and is attached to the first step, as already mentioned. Still in this tab, there must be created two predefined fields, one to take into consideration the ambient temperature — just like in the HT analysis —, and another, appended to the dynamic step, to account for the temperature change that comes as an output of the HT analysis.

The fourth, and last change, from the copied LBA to this GMNIA is in the keywords. Removing the piece of script that asks for the deformed shape to be stored in a specific file, whilst adding a piece of script to import the LBA displacements and rotations as imperfections, just like was done in the ambient temperature counterpart.

The deformed configuration of a model tested in ambient temperature is shown in Fig. 10.

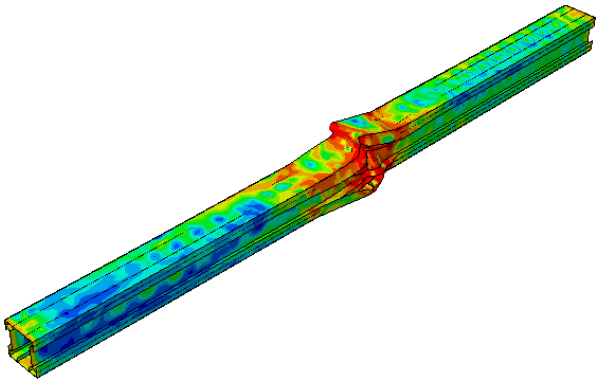

Figure 10 — Column after elevated temperature compression

4 DISCUSSION OF RESULTS

4.1 Tests results

Figure 11 shows the observed buckling modes for the built-up short columns. As anticipated, local buckling was the dominant buckling mode, but it was not clear to identify where the phenomenon started, because the specimens were inside the furnace. The only clear conclusion is that the local buckling started between fasteners. Since there was no evidence of fastener damage in any of the tested specimens, it can be concluded that the fasteners effectively reduced distortional buckling phenomenon where they were located during the fire resistance test — one fact that evidences the important role of the connectors. Significant deformations are identified for the external plain channels (U profiles). Deformation by compatibility occurred in the connected overlapping steel plates. No global buckling was identified.

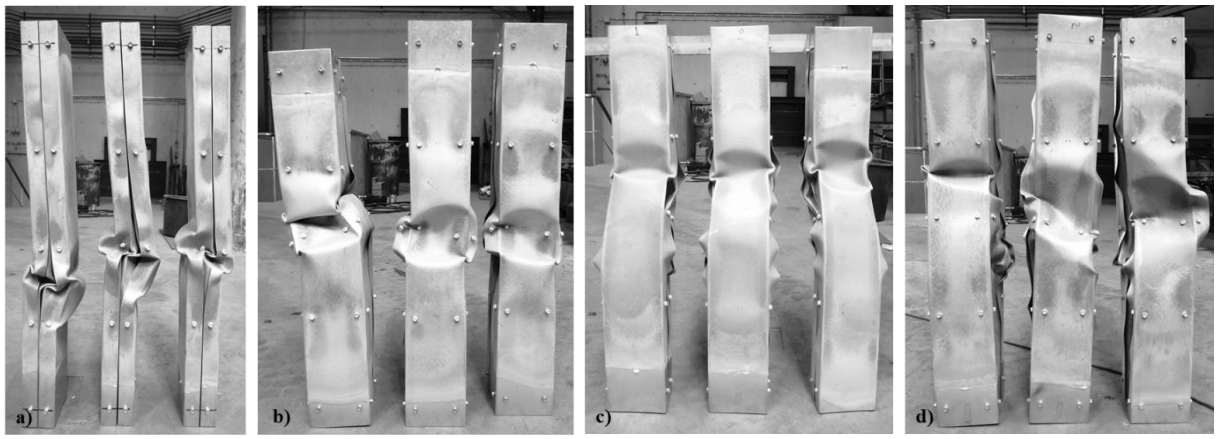

Figure 11 — Specimens deformed after the fire resistance test

Both experimental and numerical temperature evolution are in reasonable agreement — Graph 4 —, considering the adopted strategies and assumptions for the heat transfer analysis described at Subchapter 3.2.

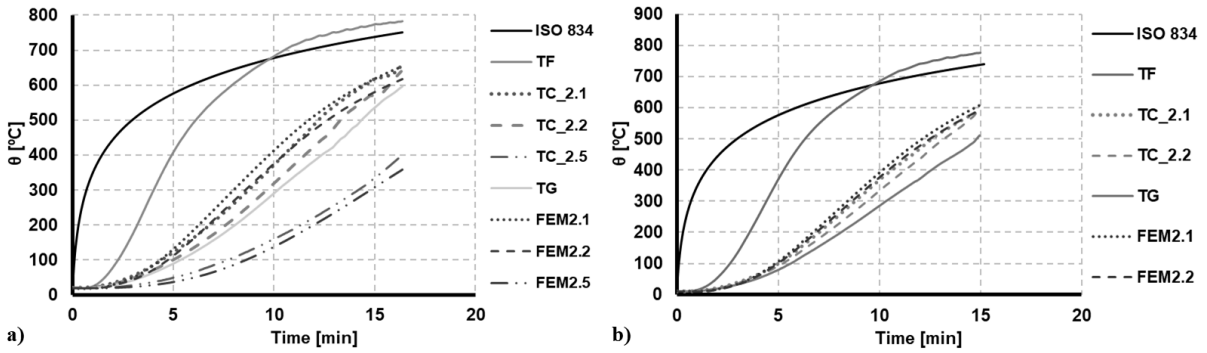

Graph 4 — Measured temperature evolution (Craveiro et. al, 2022a)

For the data present in Table 16, the critical temperature (and time) was the highest one amongst the temperatures collected in the cross-section. Worth noting that, for a $0.4N_{b,Rd}$, the critical temperatures measured were strongly higher than the recommended 350 °C of the EN 1993-1-2:2005, for class 4 cross-sections.

Table 16 — Summary of the fire resistance tests results (Craveiro et al., 2022a)

Section	P_0 *[kN]*	t_{cr} *[min]*	θ_{cr} *[ºC]*	*Section*	P_0 *[kN]*	t_{cr} *[min]*	θ_{cr} *[ºC]*
R-2C+2U_1	102.0	14.78	542	*R-2Σ+2U_1*	124.0	15.90	584
R-2C+2U_2		14.71	558	*R-2Σ+2U_2*		16.40	596
R-2C+2U_3		14.31	555	*R-2Σ+2U_3*		16.40	640
$\bar{X}$		14.6	551.7	$\bar{X}$		16.2	606.7
σ		0.2	6.9	σ		0.2	24.1
COV		1.4	1.3	*COV*		1.5	4.0
Section	P_0 *[kN]*	t_{cr} *[min]*	θ_{cr} *[ºC]*	*Section*	P_0 *[kN]*	t_{cr} *[min]*	θ_{cr} *[ºC]*
S-2C+2U_1	96.4	13.78	517	*S-2Σ+2U_1*	123.6	14.20	575
S-2C+2U_2		14.50	538	*S-2Σ+2U_2*		14.00	563
S-2C+2U_3		15.30	561	*S-2Σ+2U_3*		14.90	562
$\bar{X}$		14.5	538.7	$\bar{X}$		14.4	566.6
σ		0.6	18.0	σ		0.4	5.6
COV		4.3	3.3	*COV*		2.7	1.0

As mentioned at Subchapter 3.3, numerical models were used to reproduce the results, coming in good agreement with the experimental ones. Thus, the broader parametric studies were enabled.

4.2 Numerical models results

After running 80 Abaqus models, the force-displacement curves were made to compare each spacing for given column configuration and can be seen in the Annex (Annex Graphs 1 and 2). Throughout all configurations — combination of cross-section and length —, the maximum compression force in the s0 fastener's spacing is considerably higher. Then, it drops at suddenly when the spacing start to increase, but this decrease in maximum force soothes when the spacing gets closer to the maximum adopted.

Also, force-temperature curves were made to compare each spacing for given column configuration and load level (Annex Graphs 3 to 6). It can be seen that, for each configuration, the critical temperature is virtually the same, which was expected from the adopted strategy of loading the fire models to generate common utilization degrees.

Lastly, a virtual specimen was chosen to illustrate the force-displacement behavior through the temperature changes.

To illustrate the shortenings and expansions, during the loading phase and subsequentially heating, a virtual specimen was chosen and depicted, showing its force-displacement, and displacement-time relations. In Graph 5, it is clear to identify the loading phase — corresponding to the general static step of the GMNIA (fire), at Subchapter 3.3.2.3 —, the heating and expansion under the service load, the brief shortening before the collapse, and the collapse itself.

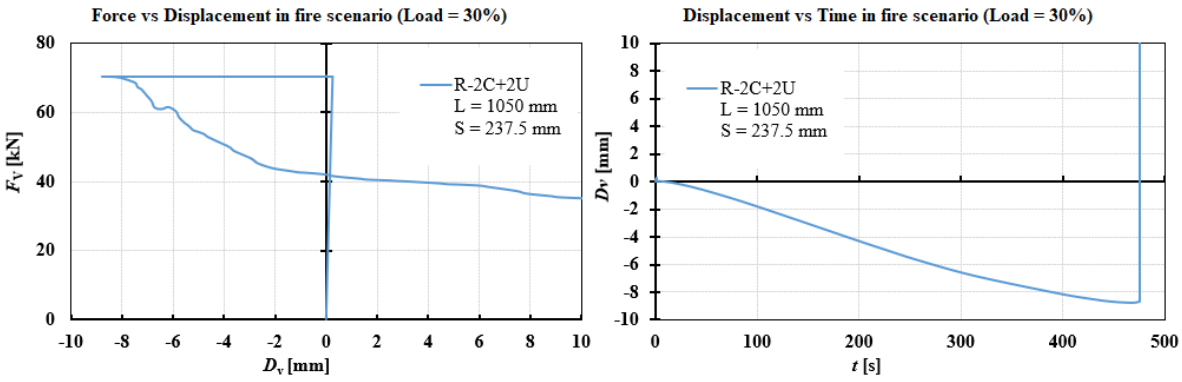

Graph 5 — Results for the R-2C+2U_s237 specimen at elevated temperature with 30% load level

Summarizing the most important information of this compilation of graphics in tables (Table 17 to 19):

Table 17 — Parametric results for ambient temperature

Cross-section	*L [mm]*	*S [mm]*	*Ambient temperature*		*Cross-section*	*L [mm]*	*S [mm]*	*Ambient temperature*	
			$P_{u,FEM,max}$ *[kN]*	$D_{v,max}$ *[mm]*				$P_{u,FEM,max}$ *[kN]*	$D_{v,max}$ *[mm]*
R-2C+2U	1050	0	299.26	1.57	R-2Σ+2U	1050	0	310.50	1.57
		118.75	241.76	1.47			118.75	284.00	1.38
		190	233.28	1.34			190	274.80	1.33
		237.5	234.13	1.31			237.5	270.48	1.41
		475	226.62	1.32			475	267.41	1.31
	3000	0	175.30	2.00		3000	0	192.35	2.10
		145	154.80	2.00			145	173.86	2.10
		290	147.56	2.00			290	169.41	2.10
		580	142.63	1.75			580	160.03	2.10
		1450	119.65	1.69			1450	121.45	1.42
S-2C+2U	1050	0	324.20	2.83	S-2Σ+2U	1050	0	378.34	3.65
		118.75	246.34	1.38			118.75	310.55	1.75
		190	241.67	1.47			190	301.63	1.81
		237.5	236.91	1.38			237.5	295.42	1.75
		475	232.96	1.35			475	283.63	1.59
	3000	0	271.89	3.45		3000	0	289.49	3.78
		145	226.26	3.20			145	263.67	3.28
		290	212.63	2.93			290	253.94	2.98
		580	210.78	2.84			580	246.05	3.04
		1450	203.86	2.78			1450	230.57	3.03

Table 18 — Parametric results for elevated temperature at 30% load level

Cross-section	*L [mm]*	*S [mm]*	*Elevated temperature - 30% load level*				
			P_{SL} *[kN]*	θ_{max} *[°C]*	*Fire resist. [s]*	$D_{v,shortening}$ *[mm]*	$D_{v,expansion}$ *[mm]*
R-2C+2U	1050	0	89.78	573.46	479.75	0.31	8.72
		118.75	72.53	576.07	478.16	0.26	8.94
		190	69.99	576.78	485.84	0.26	9.06
		237.5	70.24	574.60	475.58	0.26	9.04
		475	67.99	573.19	479.23	0.25	9.01
	3000	0	52.59	582.93	482.03	0.53	27.99
		145	46.44	584.70	479.20	0.48	28.08
		290	44.27	590.90	491.18	0.46	28.43
		580	42.79	588.83	491.61	0.45	28.40
		1450	35.90	592.69	500.36	0.38	28.77
S-2C+2U	1050	0	97.26	568.80	450.52	0.35	8.13
		118.75	73.90	576.91	464.83	0.29	8.73
		190	72.50	576.96	464.93	0.28	8.83
		237.5	71.07	576.77	464.58	0.28	8.83
		475	69.89	579.18	468.86	0.28	8.89
	3000	0	81.57	584.59	478.92	0.80	26.72
		145	67.88	576.93	464.94	0.72	26.72
		290	63.79	576.94	464.89	0.70	26.76
		580	63.23	580.17	470.68	0.69	27.05
		1450	61.16	582.83	475.52	0.66	27.38
R-2Σ+2U	1050	0	93.15	573.75	459.29	0.31	8.79
		118.75	85.20	575.09	461.68	0.28	8.97
		190	82.44	574.89	461.32	0.27	9.05
		237.5	81.14	579.96	470.29	0.27	9.14
		475	80.22	573.59	459.02	0.27	9.05
	3000	0	57.71	584.77	479.32	0.55	28.01
		145	52.16	590.65	490.65	0.50	28.42
		290	50.83	578.04	466.67	0.48	27.67
		580	48.01	596.35	501.95	0.46	28.83
		1450	36.44	595.32	499.79	0.35	29.01
S-2Σ+2U	1050	0	113.50	566.80	446.93	0.40	7.83
		118.75	93.17	575.97	463.12	0.33	8.67
		190	90.49	571.30	454.86	0.33	8.74
		237.5	88.63	574.38	460.31	0.32	8.83
		475	85.09	576.77	464.54	0.31	9.01
	3000	0	86.85	573.23	458.03	0.87	25.88
		145	79.10	574.92	461.13	0.81	26.44
		290	76.18	578.37	467.42	0.79	26.81
		580	73.81	576.07	463.22	0.76	26.89
		1450	69.17	578.00	466.75	0.72	27.27

Table 19 — Parametric results for elevated temperature at 50% load level

Cross-section	*L [mm]*	*S [mm]*	*Elevated temperature - 50% load level*				
			P_{SL} *[kN]*	θ_{max} *[°C]*	*Fire resist. [s]*	$D_{v,shortening}$ *[mm]*	$D_{v,expansion}$ *[mm]*
R-2C+2U	1050	0	149.63	447.77	313.88	0.53	6.21
		118.75	120.88	448.03	311.62	0.45	6.37
		190	116.64	448.40	314.52	0.44	6.47
		237.5	117.07	445.82	309.48	0.44	6.43
		475	113.31	446.40	312.46	0.43	6.43
	3000	0	87.65	448.48	302.58	0.88	19.94
		145	77.40	447.46	298.95	0.82	19.88
		290	73.78	453.26	304.57	0.78	20.19
		580	71.32	450.48	303.75	0.76	20.09
		1450	59.83	451.21	305.31	0.64	20.22
S-2C+2U	1050	0	162.10	445.62	297.30	0.59	5.73
		118.75	123.17	450.52	301.99	0.49	6.24
		190	120.84	447.95	299.51	0.48	6.27
		237.5	118.46	448.08	299.63	0.48	6.32
		475	116.48	448.89	300.40	0.47	6.34
	3000	0	135.95	454.79	305.97	1.34	19.20
		145	113.13	447.86	299.48	1.21	19.19
		290	106.32	447.30	298.89	1.18	19.21
		580	105.39	447.87	299.49	1.16	19.32
		1450	101.93	451.67	303.02	1.11	19.66
R-2Σ+2U	1050	0	155.25	447.34	298.98	0.52	6.25
		118.75	142.00	447.60	299.21	0.48	6.42
		190	137.40	447.06	298.71	0.46	6.46
		237.5	135.24	451.71	303.11	0.46	6.55
		475	133.71	445.93	297.64	0.45	6.50
	3000	0	96.18	450.51	301.96	0.91	20.01
		145	86.93	453.63	304.84	0.83	20.18
		290	84.71	439.39	291.57	0.82	19.46
		580	80.02	457.09	308.21	0.77	20.43
		1450	60.73	452.33	303.69	0.59	20.33
S-2Σ+2U	1050	0	189.17	444.71	296.41	0.67	5.49
		118.75	155.28	448.40	299.90	0.55	6.14
		190	150.82	445.73	297.37	0.55	6.23
		237.5	147.71	448.00	299.52	0.53	6.32
		475	141.82	450.80	302.17	0.51	6.48
	3000	0	144.75	446.95	298.54	1.45	18.64
		145	131.83	446.95	298.31	1.36	19.02
		290	126.97	450.14	301.53	1.31	19.33
		580	123.02	446.08	297.73	1.28	19.39
		1450	115.28	444.94	296.69	1.20	19.54

Throughout the spacings, the service loads applied to the fire component of the models were calculated, based on the ambient temperature baring capacity, to generate the same degree of utilization, therefore a similar critical temperature. Hence, to better understand the influence of the adopted fasteners spacing, it was made a graph (Graph 6) showing the average reduction on the column's resistance, based on the spacing — represented as a percentage of the available length, explained at Subchapter 3.3.

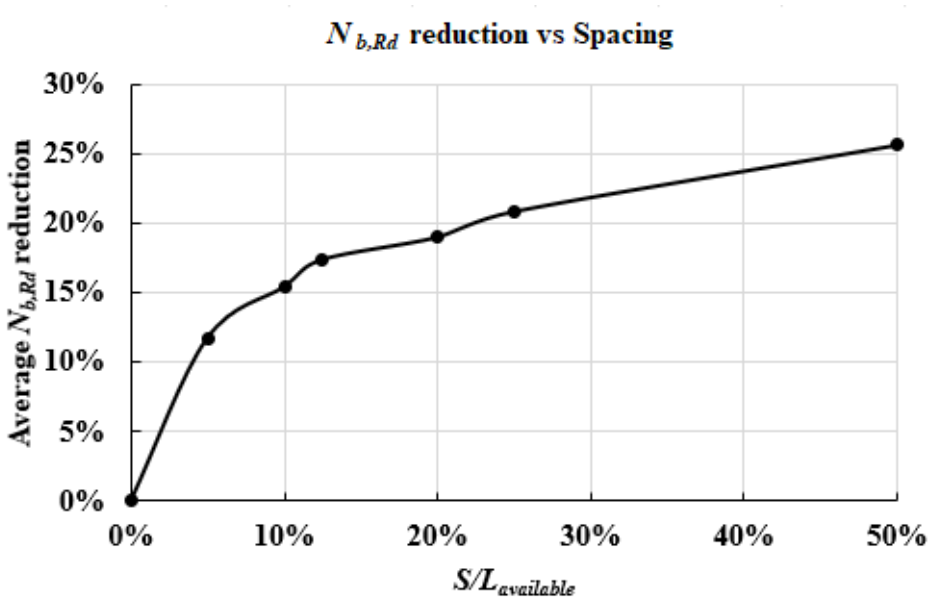

Graph 6 — Load bearing capacity reduction with spacing (ambient temperature)

Reiterating, this reduction carries over to the elevated temperature scenario. For each column configuration (cross-section and length), the critical temperature is virtually the same, offering a base of comparison among the spacings. The service load that makes the column collapse at said temperature ($N_{b,Rd,\vartheta}$) is a percentage of the depicted $N_{b,Rd}$ — 30 or 50% —, so Graph 12 do represent the shape of the load bearing reduction at elevated temperatures.

As seen, the resistance rapidly decreases as the distance between connectors start to grow, but then tends to ease into lower reductions once the spacing is bigger, like depicted in Graph 7.

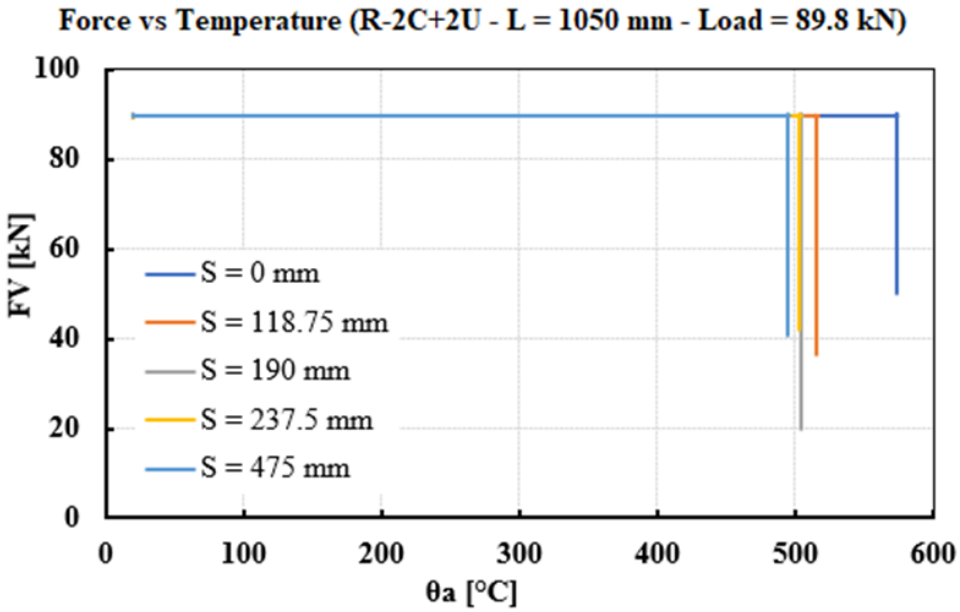

Graph 7 — Load bearing capacity reduction with spacing (elevated temperature)

Graph 7 shows, in a more direct way the decrease in resistance with the spacing. Instead of fixating the temperature and analyzing the reduction in load bearing capacity — as shown in Graph 6 —, the load was fixed and the reduction in critical temperature can be analyzed.

Regarding the influence of slenderness (Graph 8), it was analyzed how it would impact the columns' resistance at elevated temperatures. Similar to what Yang (Yang et al., 2023) did on his multitude of stationary models, the relation between the load bearing capacity in fire situation ($N_{b,Rd,\theta}$) and cross-sectional strength in fire situation ($\left[A_{eff}f_y\right]_\theta$), was put against the nondimensional slenderness in fire situation ($\bar{\lambda}_\theta$), for the present transient models. To clarify, the ratio $N_{b,Rd,\theta}/\left[A_{eff}f_y\right]_\theta$ can be rewritten to $N_{b,Rd,\theta}/A_{eff}f_y k_{y,\theta}$, and looking at Eq. 12, this fraction is equal to $\chi_{fi,\theta}$, which is the reduction factor for flexural buckling in the fire design situation.

According to the EN 1993-1-2:2005 methodology, to get to $\chi_{fi,\theta}$, it is necessary to input reduction coefficients. Likewise, the same applies to find $\bar{\lambda}_\theta$ from $\bar{\lambda}_{20}$. As listed at Subchapter 3.3.2.2, Craveiro (Craveiro et al., 2016b) studied the S280Gd+Z and proposed an alternative set of factors to the Eurocode ones. Craveiro's factors were used in this analysis because they

were also used in the parametric studies, so, to use the Eurocode's factors in this analysis would be to compare different things.

The represented points are the columns of each combination of cross-section and height. The critical temperature of these elements was used to determine the reduction coefficients and the service load that they bore is the $N_{b,Rd,\theta}$ — in which θ is θ_{cr}. This load was then combined with the cross-section's information, through Eq. 12, to yield the vertical axes of the graphs, and through Eq. 16, to yield the horizontal axes. In the other hand, the theoretical line can be drawn from the Eq.13 – 16.

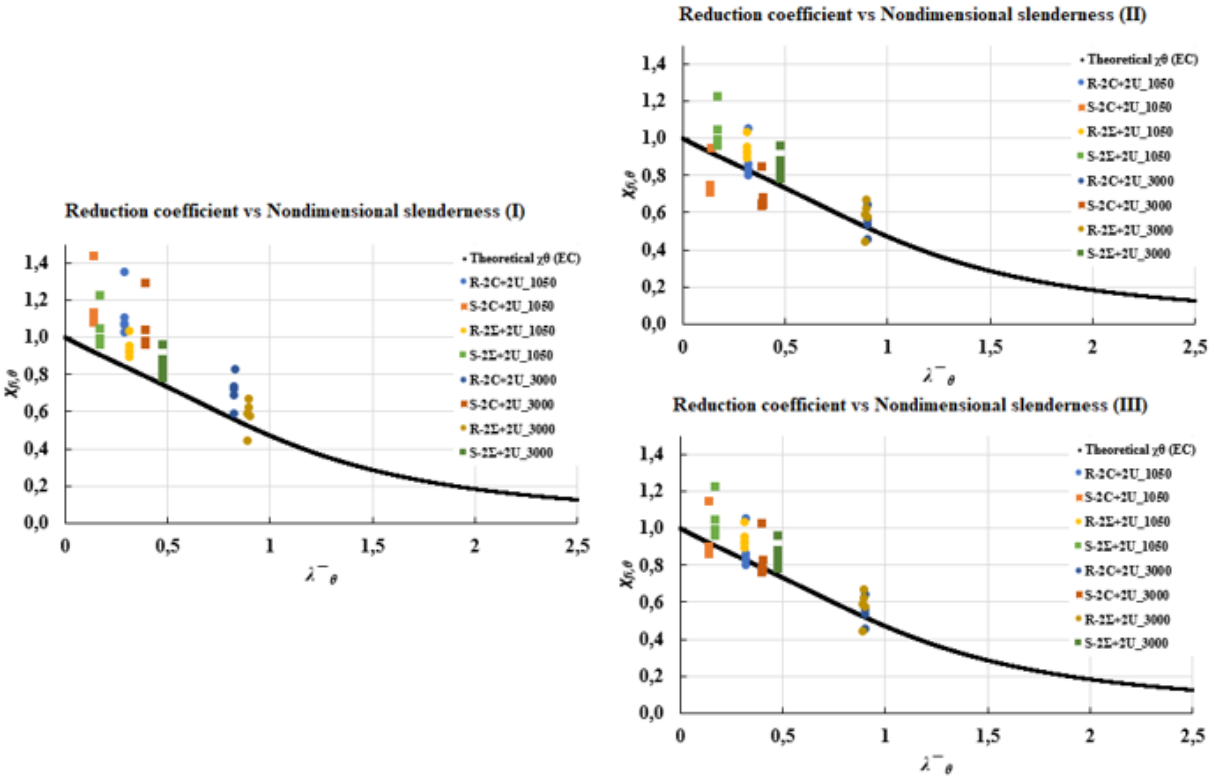

Graph 8 — Relation between the buckling reduction coefficient for elevated temperatures and the nondimensional slenderness

Three approaches were used in the plot, regarding effective properties since there is no clear indication on the Eurocode for CFS built-up cross-sections. The first was the safest and most intuitive, calculating the effective area of each channel alone and then summing, hence, ignoring the positive interaction between them. The second was considering that, for S-2R+2C cross-sections, each channel offers some kind of local bracing for adjacent ones and the lengths susceptible to buckle were the portions with no overlapping. The third was considering that, for S-2R+2C cross-sections, each channel offers some kind of local bracing for adjacent ones and the lengths susceptible to buckle were the portions between fasteners. Both the second and the

third took equally advantage of the positive interaction between overlapping in the R-2C+2U cross-sections. Figure 12 helps to better illustrate the difference between approaches II and III, with an example for part of an S-2C+2U cross-section.

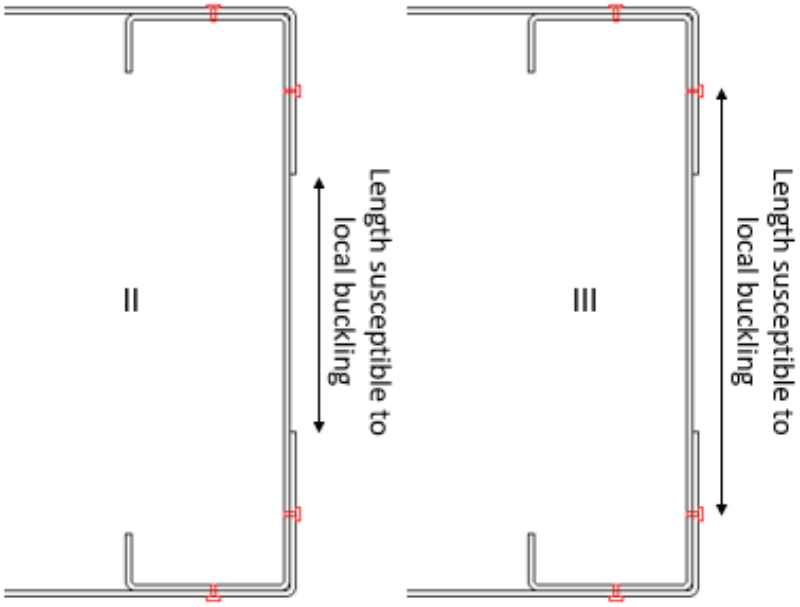

Figure 12 — Illustration of the difference between effective area calculation approaches

Regarding the cross-sections with Σ-profiles, it was simply considered that there was no reduction in area, because the overlapping sections are small. This hypothesis may require further investigation.

As seen in Graph 14, the approach I lays above the theoretical line, which means, mathematically, that the ratio "buckling resistance at elevated temperatures per sectional resistance at elevated temperatures" is bigger than 1.0 in many cases. Physically, it means that the sectional resistance is being undervalued, which is expected, since the effective area was calculated much on the safe side. Analyzing approach II, several points representing S-2C+2U lay below the theoretical line, which means that the effective area is being overvalued, *i.e.*, the effective properties were bigger than what theory suggests (falling in the unsafe side). Finally, with approach III it is seen a good agreement between the theoretical line and the plot, suggesting that the effective areas were calculated reasonably and no advantage — or disadvantage — was taken over the cross-section capabilities.

In general, since there is no method for varying the slenderness with spacing, all points representing the different spacings for a certain configuration fall almost in the same vertical line (the abscissa does not change). For a given configuration, the points with lower ordinates are the ones with higher spacing. The reason is, reverting to the ratio, that the same sectional resistance is stipulated, but the buckling resistance is lower. For higher spacings, distortional

buckling can play a huge role in lowering the resistance, but this is not being considered with this method deriving from the Eurocode.

At last, it is important to state that the conclusions are as robust as the number of tests carried out.

5 COMPARISON TO THE EUROCODE

With the tools provided by the EN 1993-1-2:2005, and described at Subchapter 2.3.2, it is possible to estimate the load bearing at ambient temperature, then the critical temperature of the element, based on the iterative process that considers the variation of the quantities according to the temperature.

As mentioned at Subchapter 2.3.1, the Eurocode does not have a mechanism to integrate the spacing of fasteners nor the degree of connection between plates in the problem. So, by the information provided by the Eurocode, it is assumed a perfect degree of connection. As such, the Eurocode's calculations will be compared to the FEM results representing the columns configurations with perfect connection (spacing 0,0 mm). It does not have clear indication regarding the effective properties of CFS built-up cross-sections, so they were calculated individually for each channel and then summed for the cross-section (as presented in approach I discussed at the last part of Subchapter 4.2).

The fire results achieved with the FEM analysis are the basis of comparison to the four approaches studied under the Eurocode method, varying the reduction coefficients and the load magnitude (Table 20)

- $EC_{coeff\_HC,load\_EC}$ uses the reduction coefficients proposed by Craveiro (Craveiro et al., 2016b), illustrated in Table 20, and the applied load calculated by the Eurocode — $N_{b,Rd,EC}$;
- $EC_{coeff\_EC,load\_EC}$ uses the reduction coefficients proposed by the Eurocode, also illustrated in Table 20, and the applied load calculated by the Eurocode — $N_{b,Rd,EC}$;
- $EC_{coeff\_HC,load\_FEM}$ uses the reduction coefficients proposed by Craveiro, and the applied load resulting from the FEM analysis — $N_{b,Rd,FEM(s0)}$;
- $EC_{coeff\_EC,load\_FEM}$ uses the reduction coefficients proposed by the Eurocode, and the applied load resulting from the FEM analysis — $EC_{coeff\_EC,load\_FEM(s0)}$.

Table 20 — Comparison of the Eurocode's predictions to FEM calculations

L [mm]	$N_{b,Rd,FEM}$ [kN]	$N_{b,Rd,EC}$ [kN]	$\theta_{max,30\% \text{ load level}}$ [°C]					$\theta_{max,50\% \text{ load level}}$ [°C]				
			FEM	$EC_{coeff\_HC,\ load\_EC}$	$EC_{coeff\_EC,\ load\_EC}$	$EC_{coeff\_HC,\ load\_FEM}$	$EC_{coeff\_EC,\ load\_FEM}$	FEM	$EC_{coeff\_HC,\ load\_EC}$	$EC_{coeff\_EC,\ load\_EC}$	$EC_{coeff\_HC,\ load\_FEM}$	$EC_{coeff\_EC,\ load\_FEM}$
R-2C+2U_1050	299,3	193,2	573,5	664,7	655,6	599,1	589,5	447,8	587,2	578,1	506,6	497,1
R-2C+2U_3000	175,3	121,0	582,9	667,4	630,3	617,2	579,2	448,5	596,4	558,8	529,5	487,2
S-2C+2U_1050	324,2	213,4	568,8	664,2	660,2	600,6	596,4	445,6	585,8	581,8	509,6	505,7
S-2C+2U_3000	271,9	179,9	584,6	665,2	651,7	604,1	590,0	454,8	588,5	575,1	513,3	499,9
R-2Σ+2U_1050	310,5	258,1	573,7	664,8	654,7	637,7	627,1	447,3	587,5	577,4	556,4	547,1
R-2Σ+2U_3000	192,4	152,3	584,8	667,7	627,3	666,4	626,9	450,5	597,9	556,5	597,8	555,5
S-2Σ+2U_1050	378,3	284,5	566,8	664,3	659,4	621,4	616,2	444,7	586,1	581,2	537,0	532,5
S-2Σ+2U_3000	289,5	228,7	573,2	665,6	647,7	631,7	612,9	447,0	589,7	572,1	549,4	533,1
Avg. diff. to FEM (%)	—	-27,2	—	15,5	12,6	8,0	5,0	—	31,6	27,8	19,9	16,0

This multitude of configurations studied, and variations adopted permit the drawing of clear conclusions about both components of the Eurocode's calculation mechanism: ambient temperature load prediction and critical temperature prediction.

The first, regarding ambient temperature load bearing capacity, points to something that is almost a consensus between researchers: the Eurocode is overconservative — *e.g.* Ellobody and Young (Ellobody and Young, 2005), Huang (Huang et al., 2021), and Craveiro (Craveiro et al., 2014). The Eurocode predicts load capacities substantially lower than the ones obtained with the FEM, on average -27.3%.

The second, regarding elevated temperatures, is that, based on the applied load provided the Eurocode, the collapse temperature is substantially higher than the one obtained the FEM — which indicates a service load prediction that is too low. However, when applying the load calculated with the FEM, this difference drops, *i.e.*, the FEM calculated service load yields better results than the Eurocode's load prediction. But this reduction is still not enough, as seen, for instance, in the 16.0% difference between the FEM critical temperature at a 50% load level and the $EC_{coeff\_EC,load\_FEM}$ at the same load level. So, it is possible to state that the fire resistance calculation mechanism is not accurate enough, especially for higher load levels — it is better calibrated for lower load levels. That is because, when fed the Eurocode load prediction, the iterative mechanism outputs bad critical temperature predictions, which can be attributed in large part to the ambient temperature bad prediction. But when fed the FEM calculated load, the iterative mechanism outputs moderate predictions, and for that there is no other component to blame.

Summarizing, the ambient temperature part of the method is not good (overconservative), and the elevated temperature part of the method is not good enough (underconservative). That is why, the EN 1993-1-2:2005, in its Clause 4.2.3.6, recommends limiting the critical temperature of class 4 cross-sections to 350 °C — which is considerably low on the safety side, as evidenced by the FEM calculations.

Must be noted that, at first, it was not expected for the calculations using Craveiro's coefficient to yield worse results than the calculations using the Eurocode's coefficients. Upon further investigation, it was identified that what matters for the temperature iterative mechanism is the relation between coefficients — the square root of the ratio between them, to be precise —, not specifically the reduction coefficients themselves. As seen in Graph 9, the Eurocode's relation is significantly higher in the temperature span of 500 °C to 700 °C, which, according to Eq. (16), increases the non-dimensional slenderness for the given temperature. Hence, the critical temperature drops. So, even though Craveiro's coefficients perform better at tests, it is not as

fitting for the Eurocode's methodology — said methodology that has already been put in question in the previous paragraphs.

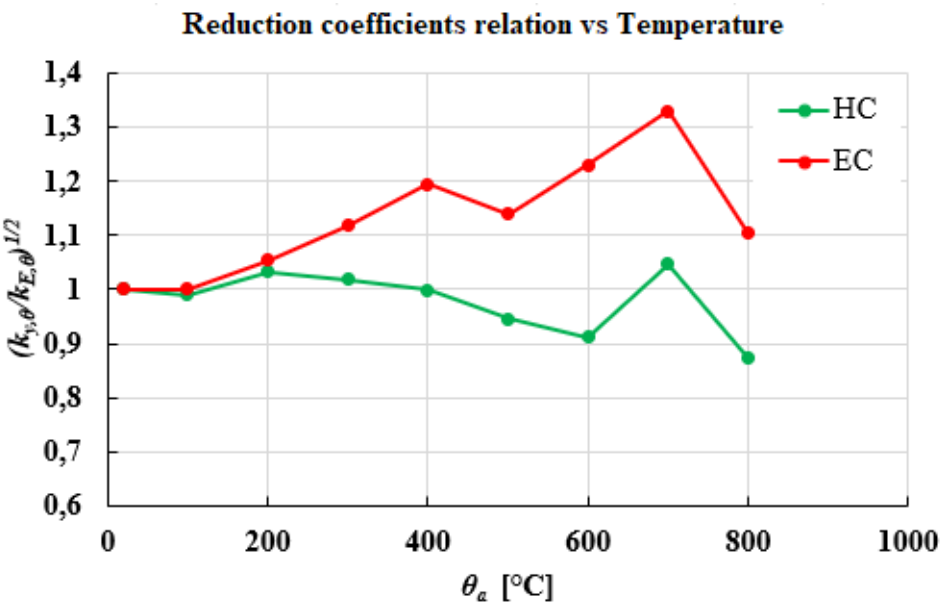

Graph 9 — Relation between reduction factors for elevated temperatures

6 CONCLUSIONS AND FUTURE WORK

A series of parametric numerical analyses on closed built-up cold-formed steel columns under fire condition was conducted. Four different cross-sections, comprised of three individual shapes — C, U and Σ —, resulted in 80 configurations according to the varying parameters: cross-section, length, spacing and load level. It was also presented the results of the experimental campaigns, both at ambient and elevated temperatures, that laid the foundation for the present numerical investigation models to be created. They characterized the material — S280Gd+Z —, measured the imperfections and observed the behavior of this type of column under compression.

The main goal was to dive further into the role that fasteners spacing plays in the load bearing capacity at elevated temperatures. To assess this topic, ambient temperature models were made for all column configurations and the $N_{b,Rd}$ was calculated. The columns were, then, loaded with a service load that would make the critical temperature virtually identical for every spacing, setting a ground of comparison for them all. This way, it was possible to see, for the same temperature, how stronger were the columns with smaller spacing.

Comparing to the perfect connection, the average reduction in load bearing capacity was:

- 11.8% for the spacing equivalent to 5% of the available length;
- 15.5% for the spacing equivalent to 10% of the available length;
- 17.4% for the spacing equivalent to 12.5% of the available length;
- 19.0% for the spacing equivalent to 20% of the available length;
- 20.9% for the spacing equivalent to 25% of the available length;
- 25.7% for the spacing equivalent to 50% of the available length.

Alternatively from the indirect approach of setting a service load to make every column collapse at a certain temperature and then comparing collapse loads, a more direct approach was illustrated in a small sample: for the configuration R-2C+2U_1050, every spacing was loaded with the same load and the critical temperatures were compared. The results, as expected, pointed at the same direction of reduction.

Another important objective was to see how accurate the Eurocode predictions were. This evaluation can be divided in two parts: the load bearing capacity at ambient temperature and the iterative critical temperature mechanism.

- Regarding the first, the Eurocode's prediction on $N_{b,Rd}$ are considerably inaccurate. Amongst researchers, that is consensus. The regulation underestimates the columns load bearing capacity by an average of 27.2%. That is the least reliable part of the two;
- Regarding the second, the Eurocode's iterative mechanism for elevated temperatures does not give sufficiently good predictions of the critical temperatures. Most of the blame can be attributed to the ambient temperature load prediction, but even when feeding the mechanism with accurate values of $N_{b,Rd}$, the output is not so reliable. The θ_{cr} estimative can be, at instances, 31.6% off-target, when using the Eurocode's ambient temperature capacity prediction as input, and 19.6% off-target, when using the FEM ambient temperature capacity calculation as input.

This study is a step forward in understanding how the degree of connection between channels impact the overall fire performance of a column. To build a robust base of knowledge, helping improve design regulations along the way, more configurations of columns ought to be investigated. For instance, using different individual shapes, boundary conditions, slenderness and so on.

Backing up to a wider perspective, the CFS build-up column field of study, more research on the effective properties calculation and the influence of the degree of connection at ambient temperature would be invaluable. Hence, proposing changes to the regulations to provide the much necessary clarity for the designers.

REFFERENCES

Abaqus Analysis User's Guide, 2017.

Arrais, F., Lopes, N., Real, P.V., 2021. Fire design of slender cold-formed lipped channel and sigma section members with uniform temperature under compression. Fire Safety Journal 122, 103340. https://doi.org/10.1016/j.firesaf.2021.103340

Askaripoor, T., 2018. Fire risk assessment and efficiency study of active and passive protection methods in reducing the risk of fire in a control room of at an industrial building. Health and Safety at Work Volume 8.

Craveiro, H.D., 2015. Fire resistance of cold-formed steel columns (Doctoral Thesis). Civil Engineering Department, University of Coimbra.

Craveiro, H.D., Rahnavard, R., Laím, L., Santiago, A., 2022a. Fire performance of built-up cold-formed steel columns. Presented at the SiF 2022– The 12th International Conference on Structures in Fire, The Hong Kong Polytechnic University.

Craveiro, H.D., Rahnavard, R., Laím, L., Simões, R.A., Santiago, A., 2022b. Buckling behavior of closed built-up cold-formed steel columns under compression. Thin-Walled Structures 179, 109493. https://doi.org/10.1016/j.tws.2022.109493

Craveiro, H.D., Rodrigues, J.P.C., Laím, L., 2016a. Experimental analysis of built-up closed cold-formed steel columns with restrained thermal elongation under fire conditions. Thin-Walled Structures 107, 564–579. https://doi.org/10.1016/j.tws.2016.07.001

Craveiro, H.D., Rodrigues, J.P.C., Laím, L., 2014. Cold-formed steel columns made with open cross-sections subjected to fire. Thin-Walled Structures 85, 1–14. https://doi.org/10.1016/j.tws.2014.07.020

Craveiro, H.D., Rodrigues, J.P.C., Santiago, A., Laím, L., 2016b. Review of the high temperature mechanical and thermal properties of the steels used in cold formed steel structures – The case of the S280 Gd+Z steel. Thin-Walled Structures, Elevated temperature performance of thin-walled structures 98, 154–168. https://doi.org/10.1016/j.tws.2015.06.002

Dabaon, M., Ellobody, E., Ramzy, K., 2015. Nonlinear behaviour of built-up cold-formed steel section battened columns. Journal of Constructional Steel Research 110, 16–28. https://doi.org/10.1016/j.jcsr.2015.03.007

Dar, M.A., Subramanian, N., Dar, A.R., Ghowsi, A.F., Sidiqui, F., Fayaz, S., Mir, M.S., 2020. Comparison of various shear connectors for improved structural performance in CFS concrete composite slabs. Engineering Structures 220, 111008. https://doi.org/10.1016/j.engstruct.2020.111008

Ellobody, E., Young, B., 2005. Structural performance of cold-formed high strength stainless steel columns. Journal of Constructional Steel Research 61, 1631–1649. https://doi.org/10.1016/j.jcsr.2005.05.001

EN 1993-1-1, Eurocode 3: Design of steel structures — Part 1–1: General rules and rules for buildings, 2005.

EN 1993-1-2, Eurocode 3: Design of steel structures — Part 1–2: General rules - Structural fire design, 2005.

EN 1993-1-3, Eurocode 3: Design of steel structures — Part 1–3: General rules, supplementary rules for cold-formed members and sheeting, 2006.

EN 1993-1-5, Eurocode 3: Design of steel structures — Part 1–5: Plated structural elements, 2006.

Georgieva, I., Schueremans, L., Vandewalle, L., Pyl, L., 2012. Design of Built-Up Cold-Formed Steel Columns According to the Direct Strength Method. Procedia Engineering, STEEL STRUCTURES AND BRIDGES 2012 - 23rd Czech and Slovak International Conference 40, 119–124. https://doi.org/10.1016/j.proeng.2012.07.066

Huang, Y., Chen, J., He, Y., Young, B., 2021. Design of cold-formed stainless steel RHS and SHS beam–columns at elevated temperatures. Thin-Walled Structures 165, 107960. https://doi.org/10.1016/j.tws.2021.107960

International Organization for Standardization, 2014. ISO 834-10:2014.

International Organization for Standardization, 2006. ISO 6892-1:2006.

Kherbouche, S., Megnounif, A., 2019. Numerical study and design of thin walled cold formed steel built-up open and closed section columns. Engineering Structures 179, 670–682. https://doi.org/10.1016/j.engstruct.2018.10.069

Laím, L., 2013. Experimental and numerical analysis on the structural behaviour of cold-formed steel beams subjected to fire (Doctoral Thesis). Civil Engineering Department, University of Coimbra, Coimbra.

Laím, L., Craveiro, H.D., Simões, R., Escudeiro, A., Mota, A., 2020. Experimental analysis of cold-formed steel columns with intermediate and edge stiffeners in fire. Thin-Walled Structures 146, 106481. https://doi.org/10.1016/j.tws.2019.106481

Laím, L., Rodrigues, J.P.C., da Silva, L.S., 2014. Experimental analysis on cold-formed steel beams subjected to fire. Thin-Walled Structures 74, 104–117. https://doi.org/10.1016/j.tws.2013.09.006

Le, T., Bradford, M.A., Liu, X., Valipour, H.R., 2020. Buckling of welded high-strength steel I-beams. Journal of Constructional Steel Research 168, 105938. https://doi.org/10.1016/j.jcsr.2020.105938

Meza, F.J., Becque, J., Hajirasouliha, I., 2020a. Experimental study of the cross-sectional capacity of cold-formed steel built-up columns. Thin-Walled Structures 155, 106958. https://doi.org/10.1016/j.tws.2020.106958

Meza, F.J., Becque, J., Hajirasouliha, I., 2020b. Experimental study of cold-formed steel built-up columns. Thin-Walled Structures 149, 106291. https://doi.org/10.1016/j.tws.2019.106291

Nie, S., Zhou, T., Eatherton, M.R., Li, J., Zhang, Y., 2020. Compressive behavior of built-up double-box columns consisting of four cold-formed steel channels. Engineering Structures 222, 111133. https://doi.org/10.1016/j.engstruct.2020.111133

Nie, S.-F., Zhou, T.-H., Zhang, Y., Liu, B., 2020. Compressive behavior of built-up closed box section columns consisting of two cold-formed steel channels. Thin-Walled Structures 151, 106762. https://doi.org/10.1016/j.tws.2020.106762

Phan, D.T., Mojtabaei, S.M., Hajirasouliha, I., Ye, J., Lim, J.B.P., 2020. Coupled element and structural level optimisation framework for cold-formed steel frames. Journal of Constructional Steel Research 168, 105867. https://doi.org/10.1016/j.jcsr.2019.105867

Possidente, L., Tondini, N., Battini, J.-M., 2020. Torsional and flexural-torsional buckling of compressed steel members in fire. Journal of Constructional Steel Research 171, 106130. https://doi.org/10.1016/j.jcsr.2020.106130

Rahnavard, R., Craveiro, H.D., Laím, L., Simões, R.A., Napolitano, R., 2021. Numerical investigation on the composite action of cold-formed steel built-up battened columns. Thin-Walled Structures 162, 107553. https://doi.org/10.1016/j.tws.2021.107553

Ranawaka, T., Mahendran, M., 2009. Experimental study of the mechanical properties of light gauge cold-formed steels at elevated temperatures. Fire Safety Journal 44, 219–229. https://doi.org/10.1016/j.firesaf.2008.06.006

Rasmussen, K.J.R., Khezri, M., Schafer, B.W., Zhang, H., 2020. The mechanics of built-up cold-formed steel members. Thin-Walled Structures 154, 106756. https://doi.org/10.1016/j.tws.2020.106756

Reyes, W., Guzmán, A., 2011. Evaluation of the slenderness ratio in built-up cold-formed box sections. Journal of Constructional Steel Research 67, 929–935. https://doi.org/10.1016/j.jcsr.2011.02.003

Rinchen, Rasmussen, K.J.R., Zhang, H., 2019. Design of cold-formed steel single C-section portal frames. Journal of Constructional Steel Research 162, 105722. https://doi.org/10.1016/j.jcsr.2019.105722

Veljkovic, M., Johansson, B., 2008. Thin-walled steel columns with partially closed cross-section: Tests and computer simulations. Journal of Constructional Steel Research, International Colloquium on Stability and Ductility of Steel Structures 2006 64, 816–821. https://doi.org/10.1016/j.jcsr.2008.01.038

Vitale, P., Spagnuolo, A., Lubritto, C., Arena, U., 2018. Environmental performances of residential buildings with a structure in cold formed steel or reinforced concrete. Journal of Cleaner Production 189, 839–852. https://doi.org/10.1016/j.jclepro.2018.04.088

Xiong, G., Kang, S.-B., Yang, B., Wang, S., Bai, J., Nie, S., Hu, Y., Dai, G., 2016. Experimental and numerical studies on lateral torsional buckling of welded Q460GJ structural steel beams. Engineering Structures 126, 1–14. https://doi.org/10.1016/j.engstruct.2016.07.050

Yang, J., Wang, W., Shi, Y., Xu, L., 2020. Experimental study on fire resistance of cold-formed steel built-up box columns. Thin-Walled Structures 147, 106564. https://doi.org/10.1016/j.tws.2019.106564

Yang, J., Zhou, X., Wang, W., Xu, L., Shi, Y., 2023. Fire resistance of box-shape cold-formed steel built-up columns failing in global buckling: Test, simulation and design. Thin-Walled Structures 183, 110433. https://doi.org/10.1016/j.tws.2022.110433

Yang, X., Jia, M., Shan, P., Lu, D., 2022. Experimental and numerical study on the seismic performance of rocking cold-formed steel frame. Thin-Walled Structures 180, 109797. https://doi.org/10.1016/j.tws.2022.109797

Young, H.D., Freedman, R.A., 2008. Física II — Termodinâmica e Ondas, 12ª Edição. ed. Pearson Education.

Yu, W.-W., Laboube, R.A., Chen, H., 2020. Cold-Formed Steel Design, 5th edition. ed. Wiley.

Ziemian, R.D., 2010. Technical Memoranda of Structural Stability Research Council — Appendix B.

FIGURES AND GRAPHS REFFERENCES

Figures

Figure 1a) – Boston Globe@ (2019). https://www.bostonglobe.com/metro/2019/11/27/the-unsolved-mystery-cocoanut-grove-fire/24YsmjPE5ruEpiaT5bev8O/story.html (official webpage), USA.

Figure 1b) – Sic Notícias@ (2018). https://sicnoticias.pt/pais/2018-08-25-Incendio-no-Chiado-foi-ha-30-anos (official website), Portugal.

Figure 1c) – NBC News@ (2021). https://www.nbcnews.com/slideshow/9-11-n645971 (official website), USA.

Figure 2 – Wei-Wen et al. (2020). "Cold-Formed Steel Design". Wiley, Hoboken.

Figure 3, 5 and 6 – Craveiro, H.D., Rahnavard, R., Laím, L., Simões, R.A., Santiago, A., 2022b. Buckling behavior of closed built-up cold-formed steel columns under compression. Thin-Walled Structures 179, 109493. https://doi.org/10.1016/j.tws.2022.109493

Graphs

Graph 1 – Craveiro, H.D., Rahnavard, R., Laím, L., Simões, R.A., Santiago, A., 2022b. Buckling behavior of closed built-up cold-formed steel columns under compression. Thin-Walled Structures 179, 109493. https://doi.org/10.1016/j.tws.2022.109493

Graph 2 – Craveiro, H.D., Rodrigues, J.P.C., Santiago, A., Laím, L., 2016b. Review of the high temperature mechanical and thermal properties of the steels used in cold formed steel structures – The case of the S280 Gd+Z steel. Thin-Walled Structures, Elevated temperature performance of thin-walled structures 98, 154–168. https://doi.org/10.1016/j.tws.2015.06.002

Graph 3 and 4 — Craveiro, H.D., Rahnavard, R., Laím, L., Santiago, A., 2022a. Fire performance of built-up cold-formed steel columns. Presented at the SiF 2022– The 12th International Conference on Structures in Fire, The Hong Kong Polytechnic University.

ANNEX

Numerical results graphs for ambient temperature:

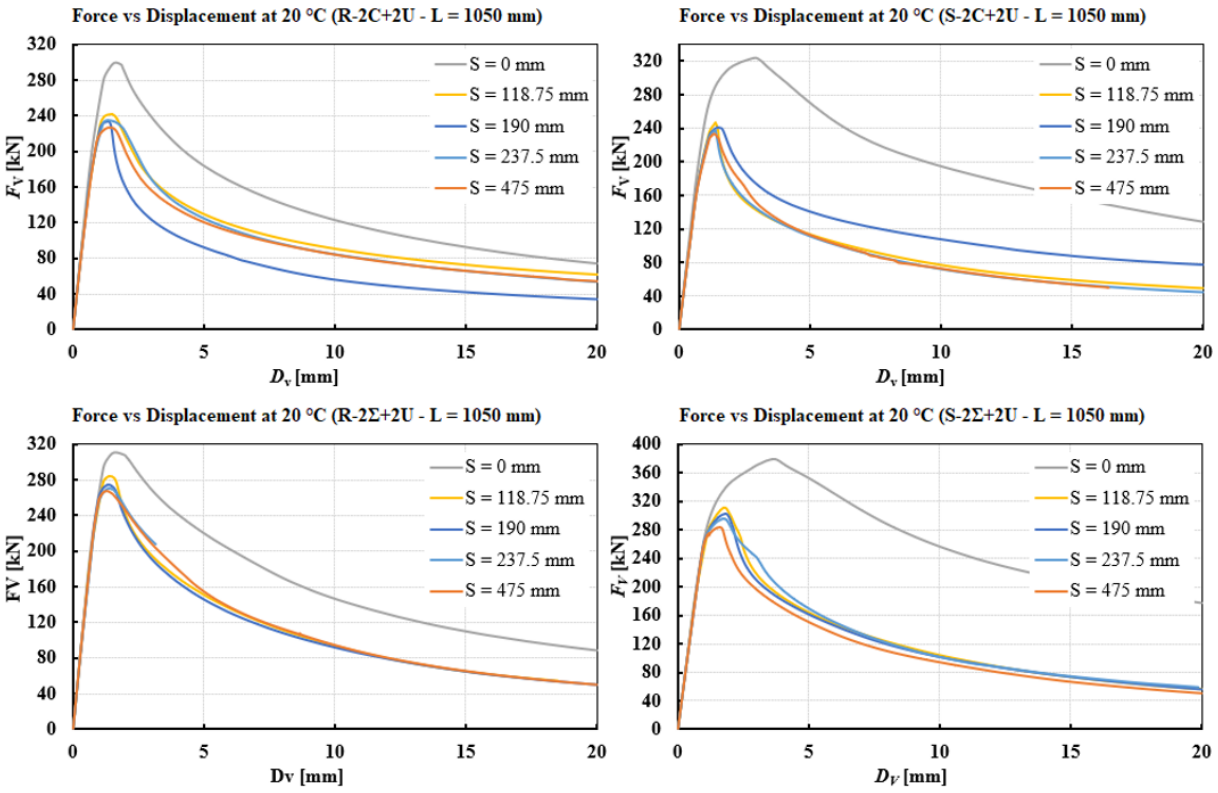

Annex Graph 1— Parametrical results for 1050 mm columns at ambient temperature

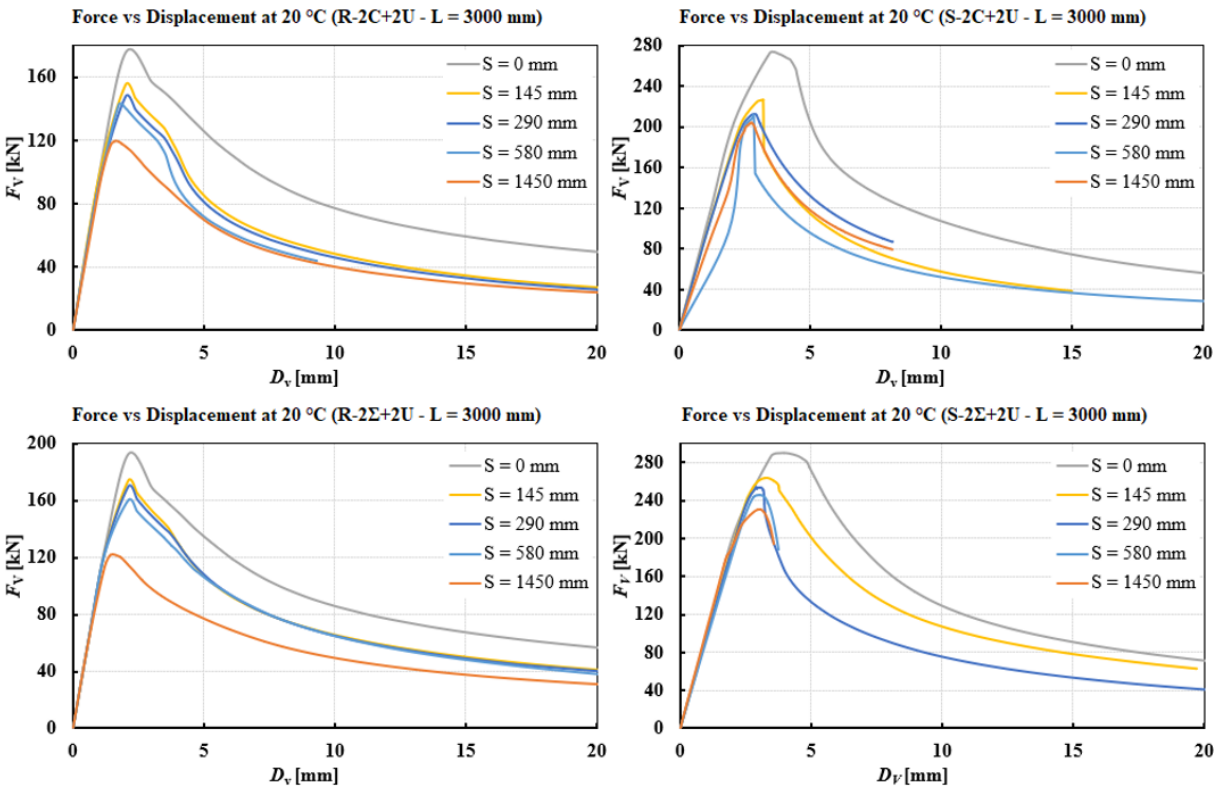

Annex Graph 2 — Parametrical results for 3000 mm columns at ambient temperature

Numerical results graphs for elevated temperatures:

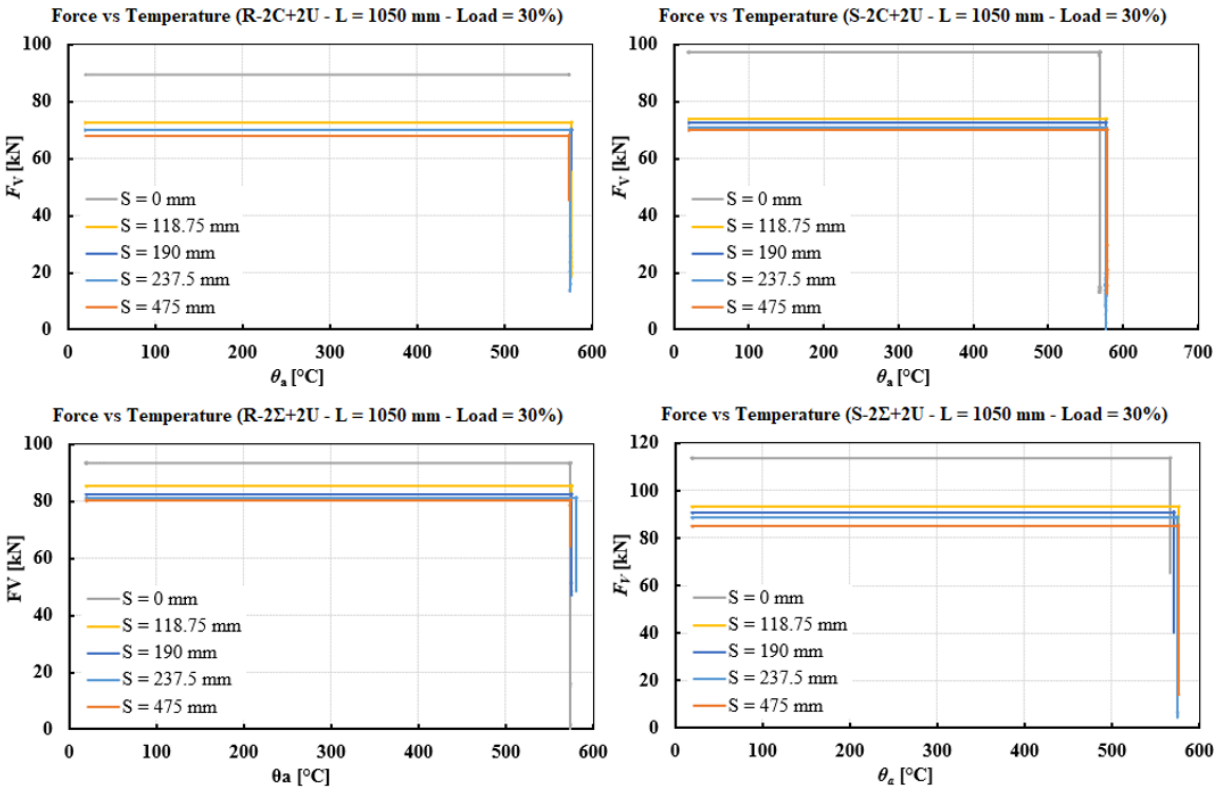

Annex Graph 3 — Parametrical results for 1050 mm columns at elevated temperature with 30% load level

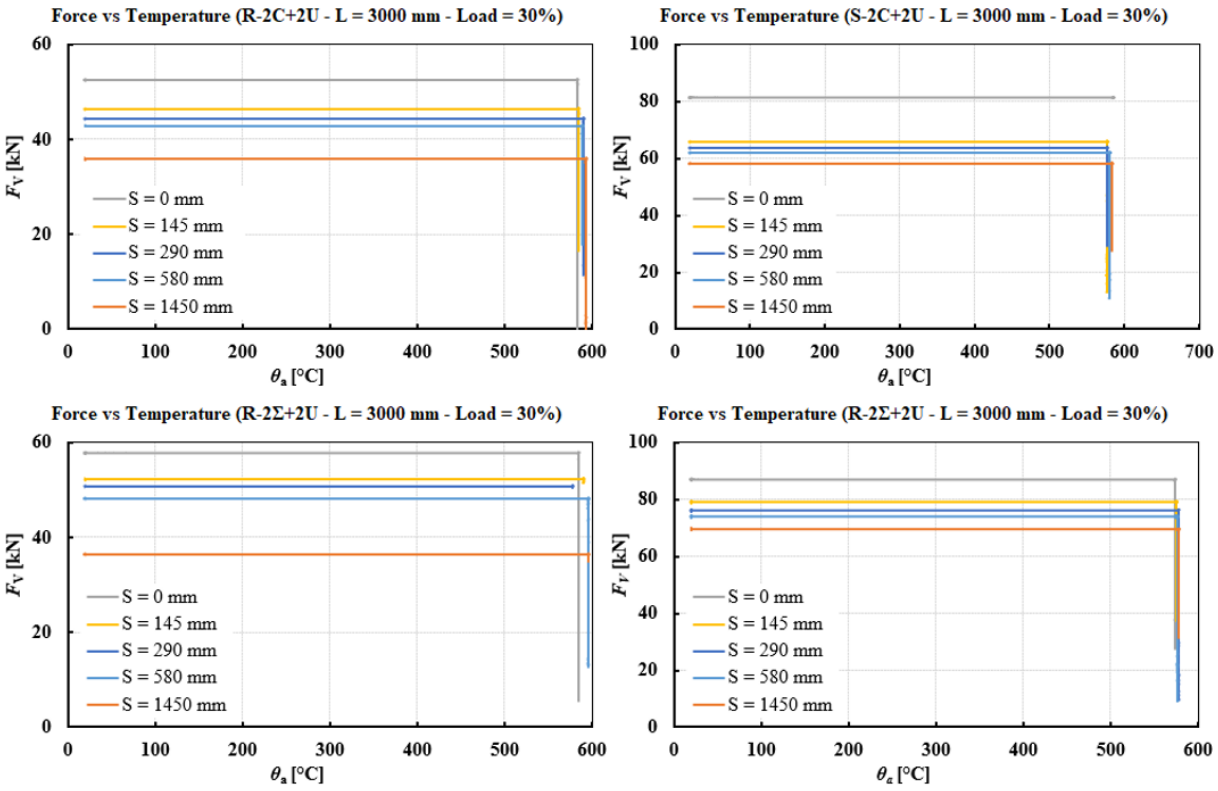

Annex Graph 4 — Parametrical results for 3000 mm columns at elevated temperature with 30% load level

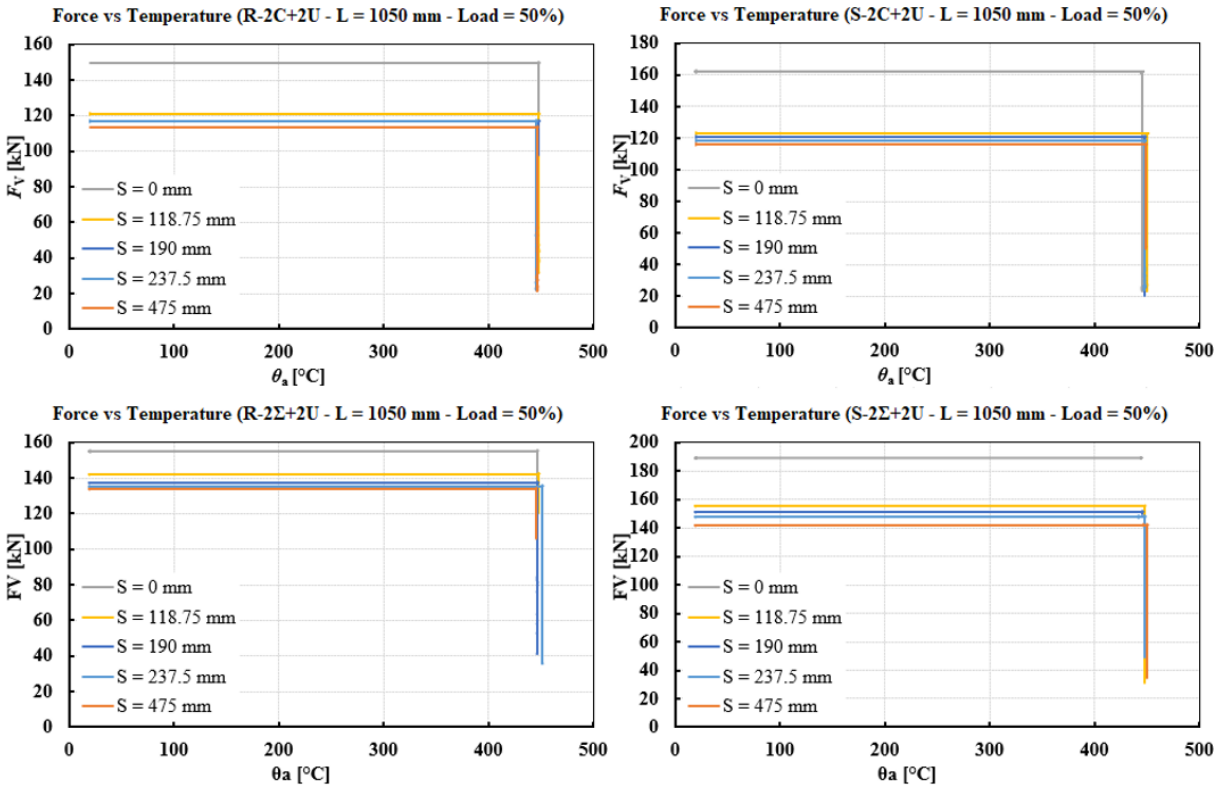

Annex Graph 5 — Parametrical results for 1050 mm columns at elevated temperature with 50% load level

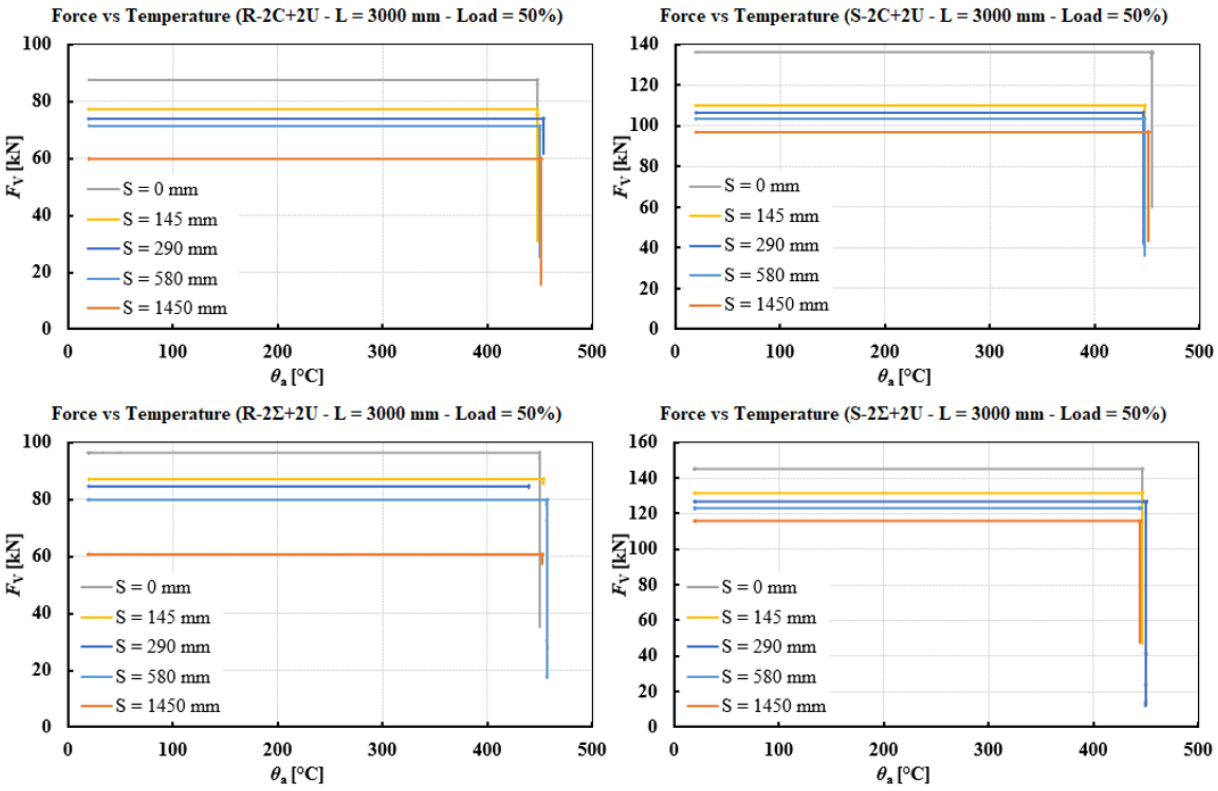

Annex Graph 6 — Parametrical results for 3000 mm columns at elevated temperature with 50% load level